U.PORTO
FACULDADE DE CIÊNCIAS
UNIVERSIDADE DO PORTO

Domain wall evolution beyond quartic potentials with GPUs and CUDA

Manuel Correia Rosa

Dissertação de Mestrado apresentada à
Faculdade de Ciências da Universidade do Porto em
Física

2020

Domain wall evolution beyond quartic potentials with GPUs and CUDA

Manuel Correia Rosa
Mestrado em Física
Departamento de Física e Astronomia
2020

Orientador
Carlos José Amaro Parente Martins
Investigador Coordenador, Centro de Astrofísica da Universidade do Porto

U.PORTO

FACULDADE DE CIÊNCIAS
UNIVERSIDADE DO PORTO

Todas as correções determinadas pelo júri, e só essas, foram efetuadas.

O Presidente do Júri,

Porto, 11 / 12 / 2020

Acknowledgements

This thesis was done under the supervision of Carlos Martins who provided me with amazing guidance and insight into the field. His flexibility to discuss any results and doubts I had, proved to be invaluable in writting this thesis and I'm very thankful for that.

To Centro de Atrofísica da Universidade do Porto for providing me with the resources (both computational and physical) to run my simulations. I would also like to thank the investigators that work there for their expertise, especially to José Correia for being an amazing physicist and friend and helping me in every step of the way whenever I needed it.

To my friends for their support and mutual inspiration and to Real Sounds Better for putting our projects on hold for a few months (sorry).

Finally I'm grateful for my parents for funding and incentivizing me to complete my studies.

Manuel Rosa

Resumo

Paredes de domínio são um tipo de defeito topológico que se pode formar durante transições de fase no Universo primordial e, visto poderem sobreviver até hoje, é importante desenvolver e aperfeiçoar modelos que consigam recriá-las para que possamos também perceber melhor como observá-las. Historicamente esta análise tem sido feita evoluindo um campo escalar confinado num potencial quártico com dois poços de potencial, mas avanços em técnicas de física computacional e em hardware (especificamente GPGPUs) permitem-nos correr um numero maior de simulações para condições diferentes mais facilmente. O objetivo desta tese é tirar proveito destes avanços em computação para estudar a evolução de paredes de domínio noutros tipos de potencial.

No primeiro capítulo estabelecemos as fundações teóricas para o nosso trabalho revendo o modelo cosmológico atual que servirá de quadro para as nossas simulações e examinamos o mecanismo por trás da formação de paredes de domínio, assim como o modelo VOS que é tipicamente usado para modelar a sua evolução.

O segundo capítulo espicifica os passos numéricos que tomámos de forma a realizar simulações de teoria de campo consistentes ao longo da tese. Serve também para testar o nosso código num potencial quártico com o intuito de validar o nosso método.

A primeira implementação para um caso diferente de ϕ^4 é feita para um potencial sinusoidal no terceiro capítulo onde é observada e discutida a formação the novos tipos de paredes exóticos e onde interpretamos os desvios em relação ao modelo prototípico e às previsões analíticas.

No quarto capítulo investigamos a formação de defeitos topológicos num potencial com três poços de potencial e extendemo-lo para interpolar entre ϕ^6 e ϕ^4. Através da introdução de um mecanismo de arrefecimento para dissipar os elevados gradientes presentes nos primeiros instantes da simulação, observa-se um decaimento do vácuo que depende da diferença de potencial, da taxa de expansão do Universo e do tempo em que deixámos o sistema "arrefecer".

Por fim, no sexto capítulo, é feita uma análise sistemática a todo o trabalho feito relacionando os vários modelos e é discutido de que forma esta análise pode ser aperfeiçada em trabalhos futuros.

Palavras-chave: Cosmologia, Física computacional, Defeitos topológicos, Paredes de domínio

Abstract

Domain walls are a category of topological defect that can form during phase transitions in the early Universe and, since they can be long-lived, it's important to develop and refine models that can produce them so we can better understand how to probe them. Historically this has been done by evolving a scalar field confined in a quartic potential with a double well, but advances in techniques for computational physics and hardware (specifically GPGPUs) have made it easier to perform a larger amount of simulations for different conditions. Our goal in this thesis is to take advantage of these advances in computation to study the evolution of domain walls in other types of potentials

In the first chapter we set the theoretical foundations for our work by reviewing the current cosmological model that will serve as the framework for our simulations and go over the mechanism behind the formation of domain walls, as well as the VOS model that typically used to model their evolution.

The second chapter details the numerical steps that we took to make consistent field theory simulations throughout this thesis. It also serves to test our code for a quartic potential in order to validate our method.

The first implementation beyond ϕ^4 is done for a sinusoidal potential in the third chapter where we observed and discussed the formation of new exotic types of walls and interpret the deviations from the prototypical model and analytical predictions.

In the fourth chapter we investigate the formation of defects in a triple well potential and extend it to interpolate to between ϕ^6 and ϕ^4. By introducing a cooling mechanism to dissipate the large gradients of the initial time steps, we observe that the field undergoes a vacuum decay that depends on the on the difference of potential, the expansion rate of the Universe and the time that we allowed cooling to occur.

Finally, in the sixth, we perform a systematic analysis of all the work done relating all models and we discuss how this analysis can be further refined in future works.

Keywords: Cosmology, Computational physics, Topological defects, Domain walls

Contents

List of Figures

List of Tables

Glossary of Symbols and Abreviations

Natural units will be used throughout this thesis where the speed of light, the reduced Planck constant and the Boltzmann constant are set to be exactly one: $c = \hbar = k_B = 1$. The metric signature is chosen to be (1, -1, -1, -1). Greek indices μ, ν,... are used to represent the space-time coordinates and run over 0, 1,..., D while latin lower case letters are used to represent spatial coordinates and run over 1, 2,..., D. Einstein notation will be used unless otherwise specified. Bold letters $\vec{x}$ are used to represent spatial vectors. Newton's notation (i.e. $\dot{x} \equiv dx/dt$) will be used in respect to physical time unless otherwise specified.

Symbol	Definition
G	Gravitational constant
Λ	Cosmological constant
a	Scale factor
t	Physical time
η	Conformal time
$T_{\mu\nu}$	Energy-momentum tensor
$g_{\mu\nu}$	Metric tensor
g	Determinant of the metric tensor
$\mathcal{L}$	Lagrangian density
S	Action
H	Hubble parameter
$R_{\mu\nu}$	Ricci tensor
R	Ricci scalar
ρ	Energy density
λ	Expansion exponent in physical time
P	Pressure
ρ_w	Wall density
σ_w	Wall energy per area
V	Total volume of space
L	Correlation length
w_0	Wall thickness
σ	Wall surface tension
γ	Lorentz factor

Abreviation	**Name**
ΛCDM	Lambda cold dark matter
FLRW	Friedmann–Lemaître–Robertson–Walker
GR	General Relativity
GUT	Grand unified theory
EOS	Equation of state
CDM	Cold dark matter
VOS	Velocity-dependent one-scale
PRS	Press-Ryden-Spergel
RMS	Root mean square
EOM	Equation of motion
GPGPU	General purpose graphics-processing-unit
MCMC	Markov Chain Monte Carlo
SG	Sine-Gordon

Chapter 1

Introduction

1.1 ΛCDM Cosmology

1.1.1 Historical context

The beginning of modern cosmology can be traced to 1915 with Albert Einstein's theory of General Relativity (GR) [12]. By 1922, the physicist Alexander Friedmann had used Einstein's theory to develop a mathematical model for a non-static Universe [14] which could imply that it expanded from a hot dense fluid into the Universe we observe today. These ideas were all based on the cosmological principle that states that, at large enough scales, the properties of the Universe are the same for all observers. Mathematically, this translates to two important fundamental properties in modern cosmology:

- Homogeneity - The Universe exhibits translational invariance;
- Isotropy - The Universe exhibits rotational invariance.

Experimentally, the idea of an expanding Universe was later corroborated by the observations made by Edwin Hubble in 1929 [18] that established a linear correlation between the receding velocity of galaxies and their distance from the observer (figure 1.1), which later came to be known as the Hubble law.

Another important experimental evidence for an Universe that expanded from a hot dense state was the discovery of the Cosmic Microwave Background (CMB) in 1965 by Penzias and Wilson [30] - electromagnetic radiation that permeates space and is a result of the recombination period when radiation decoupled from matter.

1.1.2 FLRW Cosmology

GR is the best candidate for describing gravity which is understood to be the main driver for the evolution of the Universe as a whole. In this theory, space-time is represented as a

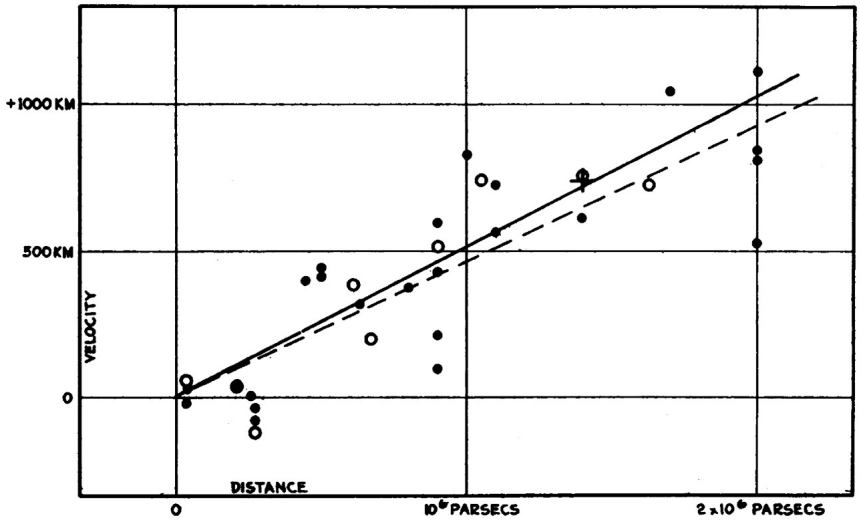

Figure 1.1: Velocity-Distance Relation among Extra-Galactic Nebulae taken from Hubble's original work [18].

4-dimensional manifold and its dynamics is encapsulated in the Einstein field equation for the metric:

$$R_{\mu\nu} - \frac{1}{2} R g_{\mu\nu} = 8\pi G T_{\mu\nu} \tag{1.1}$$

Our current understanding of the Universe suggests that, at large scales, the cosmological principle holds true. Based on this assumption, one chooses to use the Friedmann-Lemaître-Robertson-Walker (FLRW) metric with line element ds defined as

$$ds^2 = dt^2 - a\left(t\right)^2 d\vec{x}^2 \tag{1.2}$$

where $\vec{x}$ spans over the 3-dimensional space with uniform curvature parameterized by k wich, in spherical coordinates, can be written as

$$d\vec{x}^2 = \frac{dr^2}{1 - kr^2} + r^2 d\Omega^2 \tag{1.3}$$

where $d\Omega$ is the element of solid angle. From the cosmological principle, it's also reasonable to take the content of the Universe at any time to behave as an isotropic perfect fluid, which has its energy-momentum tensor defined as

$$T_{\mu\nu} = \left(P + \rho\right) u_\mu u_\nu - P g_{\mu\nu} \tag{1.4}$$

with u_μ being the fluid's 4-velocity.

By plugging the FLRW metric (1.2) and the energy-momentum tensor (1.4) in equation (1.1) and taking its 00 component and its trace we can obtain the Friedmann and Raychaudhuri

equations respectively:

$$H^2 = \frac{8\pi G}{3}\rho - \frac{k}{a^2} \tag{1.5}$$

$$\frac{\ddot{a}}{a} = -\frac{4\pi G}{3}(\rho + 3P) \tag{1.6}$$

In equation (1.5) we used the usual definition for the Hubble parameter $H \equiv \dot{a}/a$. These two equations can be manipulated and combined to give us the continuity equation for the energy density in an FLRW Universe

$$\dot{\rho} = 3H(\rho + P) \tag{1.7}$$

which, for a perfect fluid described by the EOS $P = \omega\rho$ with constant ω, has the general solution

$$\rho \propto a^{-3(1+\omega)} \tag{1.8}$$

Based on the current cosmological constraints [1] it is reasonable to assume that, at any time, the contribution of the curvature to the dynamics of the Universe is negligible compared to the energy density. This means that we can simply set $k = 0$ and solve (1.5) for a single perfect fluid using (1.8) by also fixing $a(t = 0) = 0$. This gives us an equation for the evolution of the scale factor as a function of the content of the Universe:

$$a \propto t^{\frac{2}{3(1+\omega)}} = t^{\lambda} \tag{1.9}$$

We know that, for non-relativistic matter, $\omega = 0$ and, for ultra-relativistic particles, $\omega = 1/3$. We can then create a good description of the expansion rate of the Universe when it's dominated by radiation and by non-relativistic matter:

$$a_{rad} \propto t^{1/2} \tag{1.10}$$

$$a_{mat} \propto t^{2/3} \tag{1.11}$$

1.1.3 Missing Pieces

We also know from different independent types of observations (galaxy rotation curves [37], structure formation [34], CMB [1], etc.) that the non-relativistic matter content of the Universe is mainly non-baryonic matter that only interacts with other matter through gravity. These characteristics define what is known as cold dark matter (CMD) and its relative abundance in our Universe is $\Omega_{CDM}/\Omega_{matter} = 0.8361 \pm 0.0064$ [1].

Another missing ingredient in the standard FLRW model is dark energy. Up until the late nineties, expansion was thought to either be constant or decelerated as a consequence of

gravitational attraction. However, in 1998, two independent research teams [31, 33] showed that in fact this expansion was accelerating. We can introduce an extra term Λ in Einstein's field equation (1.1) to account for that:

$$R_{\mu\nu} - \frac{1}{2}Rg_{\mu\nu} + \Lambda g_{\mu\nu} = 8\pi G T_{\mu\nu} \tag{1.12}$$

The introduction of this term is consistent with Einstein's original derivation of the field equations and an extension of the theory. Furthermore, it can also be thought of as an additional component of the energy-momentum tensor, consistent with the description of a fluid with negative pressure ($\omega = -1$).

The current measurements of the relative densities of these quantities in the Universe were taken from Planck data [1] and are $\Omega_\Lambda = 0.6834 \pm 0.0084$, $\Omega_{matter} = 0.3166 \pm 0.0084$ and $\Omega_{radiation} \sim 10^{-5}$ for a flat Universe.

Another important feature of the modern cosmology landscape is inflation - a mechanism first introduced by Alan Guth in 1981 [15] to solve several problems in the current Big Bang model by introducing a rapid exponential expansion ($a \propto \exp(t)$) period in the early Universe:

- The horizon problem - Gravitational expansion doesn't give enough time for patches of the early Universe to reach thermal equilibrium before they become casually disconnected. If this was the case we could not explain why the Universe appears homogeneous and isotropic. By introducing inflation we guarantee that these regions were casually connected in thermal equilibrium but inflation pushed them beyond the cosmological horizon eventually becoming disconnected, but maintaining the same statistical properties.

- The flatness problem - The fact that the density of matter (relativistic and non-relativistic) in the Universe is very close to the critical density necessary for a flat Universe has far-reaching implications, since any small variation of this value in the early Universe would increase rapidly over time as the density of matter decreases. During inflation, however, this value would instead decrease forcing the curvature to zero.

- The monopole problem - Magnetic monopoles are topological defects (details in the next section) that naturally arise in the early Universe in Grand Unified theories (GUT). These relics are very long lived to the point where their density would exceed the critical density of the Universe overclosing it. Despite several tests being made, no monopoles were yet observed which has placed strict limits on their density. Inflation can deal with this issue by "pushing" the monopoles out of the horizon in a similar way as in solving the horizon problem. This mechanism not only applies for monopoles but for other types of topological defects as well such as domain walls that would also end up dominating the density of the Universe if no mechanism existed to disperse them.

Table 1.1: Topological classification of defects based on the constrains on the homotopy group of the vacuum manifold $\mathcal{M}$.

Homotopy constraint	Topological Defect	Dimension
$\pi_0(\mathcal{M}) \neq \boldsymbol{I}$	Domain walls	2
$\pi_1(\mathcal{M}) \neq \boldsymbol{I}$	Strings	1
$\pi_2(\mathcal{M}) \neq \boldsymbol{I}$	Monopoles	0
$\pi_3(\mathcal{M}) \neq \boldsymbol{I}$	Textures	-

1.2 Topological Defects

The formation of domain structures is a known phenomenon in gauge theories with spontaneous symmetry breaking. It's often applied in the context of condensed matter and particle physics with consistent results. In cosmology, this mechanism was first studied by Kibble [20], in particular the topology and scale of the defects that form as a result of phase transitions in the early Universe. In many cases these defects can persist throughout the evolution of the Universe and leave its imprints as fossil relics.

A significant part of the theoretical analysis of these defects will closely follow the work presented in [35] in particular the Kibble mechanism. This mechanism produces defects when a scalar field ϕ undergoes a phase transition caused by expansion, changing the expectation value of the field $\langle\phi\rangle$. Due to gaussian fluctuations in the field and the finite correlation distance between different patches in the Universe, protodomains (and consequently topological defects) can form. The topology of these defects is only dependent on the symmetry breaking scenario. Let us suppose that ϕ obeys a symmetry defined by a group G which is broken to a subgroup K such that $G \to K$. The manifold of the new degenerate vacuum state $\mathcal{M}$ can be identified with the coset space $\mathcal{M} = G/K$. The type of topological defect that arises is shown to be related to the non-trivial n-th homotopy group of $\mathcal{M}$ as detailed in table 1.1

There are essentially two ways of approaching the nonlinear evolution of these defects. The first one is by developing a model that captures the thermodynamics of the system. This idea was first implemented by Kibble [21] for a model of string networks with a single macroscopic correlation length that characterizes the dynamics of the system. The current state of the art and the model that we will be closely following is the velocity-dependent one-scale (VOS) model that was firstly developed for strings [25, 26] and later extended to domain walls [3, 28] and monopoles [27] and gives us dynamical equations for both the correlation length and RMS velocity of the network. This model also only has two free parameters that need to be calibrated using additional computational data. This brings us to the second method of computing the evolution of topological defects which is by using high-resolution numerical simulations of field theory. This thesis will mostly focus on the latter but will mention the VOS model occasionally in order to contextualize and compare our results to the analytical predictions of the model.

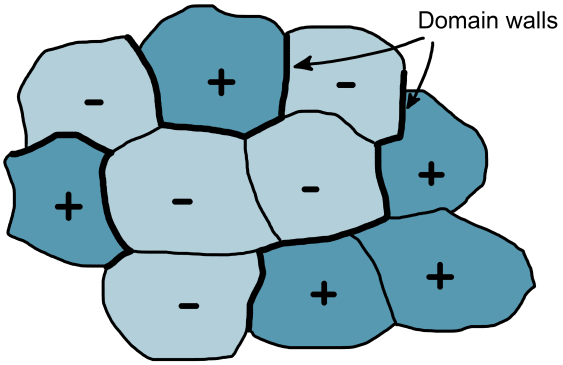

Figure 1.2: Schematic 2D representation of a system where the vacuum manifold has two disconnected regions "+" and "-" and domain walls interpolate between these two states.

1.2.1 Domain Walls

We chose to focus this work solely on the formation and evolution of domain walls. These form as a result of a discrete symmetry breaking if the vacuum manifold contains several disconnected components. Due to random fluctuations, different regions of space can assume different vacuum expectation values. Since the field is required to interpolate smoothly between these regions, domain walls form at the boundaries of domains with different vacuum expectation values as shown schematically in figure 1.2. The general model we study involves a real scalar field with a Lagrangian of the form

$$\mathcal{L} = \frac{1}{2}\partial_\mu\phi\partial^\mu\phi + V(\phi) \tag{1.13}$$

where the potential $V(\phi)$ has a discrete set of degenerate minima.

By varying the action

$$S = \int dt \int d^3x\sqrt{-g}\mathcal{L} \tag{1.14}$$

with respect to ϕ we can obtain the equation of motion for the field:

$$\frac{\partial^2\phi}{\partial t^2} + 3H\frac{\partial\phi}{\partial t} - \frac{1}{a^2}\nabla^2\phi = -\frac{\partial V}{\partial\phi} \tag{1.15}$$

It's useful to represent the equation of motion in terms of conformal time by doing a coordinate transform such that the temporal coordinate is preserved through changes in the scale factor. We define this coordinate by the relationship

$$d\eta = \frac{dt}{a(t)} \tag{1.16}$$

Using this definition, equation (1.15) becomes

$$\frac{\partial^2\phi}{\partial\eta^2} + 2\left(\frac{d\ln a}{d\ln\eta}\right)\frac{1}{\eta}\frac{\partial\phi}{\partial\eta} - \nabla^2\phi = -a^2\frac{\partial V}{\partial\phi} \tag{1.17}$$

where the term $d\ln a/d\ln\eta$ depends solely on the rate of expansion and acts like a damping mechanism in the system. In particular, for a power-law evolution of the Universe as given by (1.9), it can be shown that

$$\frac{d\ln a}{d\ln\eta} = \frac{\lambda}{1-\lambda} \tag{1.18}$$

The energy-momentum tensor for the field can also be obtain through its usual definition and is given by

$$T_{\mu\nu} = \partial_\mu\phi\partial_\nu\phi - g_{\mu\nu}\mathcal{L} \tag{1.19}$$

1.2.2 The VOS model for domain walls

The evolution of a network of domain walls can be analytically described by the VOS model [3, 28]. This model starts from the microscopic equations of motion for the walls and carries out a statistical average for the system assuming that the defects are randomly distributed at large scales. This analysis leads to a nonlinear system for the evolution of the correlation length L and the RMS velocity of the walls v.

Our derivation will closely follow the work done by Martins et al. [28]. We start by considering an infinitely thin wall parameterized by σ_1 and σ_2. This means that the evolution of the wall can be described by the smooth function $x^\mu(\eta,\sigma_1,\sigma_2)$ where we identified $\sigma_0 \equiv \eta$. We can also require two tangential vectors to be orthogonal ($\partial_{\sigma_1}x^\mu\partial_{\sigma_2}x_\mu = 0$) and the wall velocity to be normal to the tangent of the wall surface ($\partial_\eta x^\mu\partial_{\sigma_1}x_\mu = \partial_\eta x^\mu\partial_{\sigma_2}x_\mu = 0$).

To derive the EOM we start from the Dirac action for a membrane (the Nambu-Goto equivalent for walls) by firstly identifying the induced metric

$$\gamma_{ab} = g_{\mu\nu}\partial_a x^\mu\partial_b x^\nu \tag{1.20}$$

The action is then given by

$$S = -\int \mathcal{L}d^3\sigma = -\sigma_w\int\sqrt{\det(\gamma_{ab})}\,d^3\sigma \tag{1.21}$$

where σ_w is a constant mass per unit area. By computing the energy-momentum tensor and taking its 00 component we get the energy of the wall E (in a FLRW background). If we then divide it by the total volume of space V we get energy density in that volume:

$$\rho \equiv \frac{E}{V} = \frac{\sigma_w a^2}{V}\int\epsilon\,d^2\sigma \tag{1.22}$$

where the coordinate energy per unit length ϵ is defined as

$$\epsilon^2 = \frac{\vec{x}'^{\,2}}{1-\dot{\vec{x}}^2} \tag{1.23}$$

with time derivative $\dot{\vec{x}}$ in respect to conformal time and spatial derivative $\vec{x}'$, which, in our particular case, is simply $\vec{x}'^{\,2} \equiv (\partial_1 \vec{x})^2 (\partial_2 \vec{x})^2$.

We can also apply standard variational methods to (1.21) in order to obtain the EOM for the wall:

$$\frac{\partial_\eta a}{a} \delta_{0\lambda} \sqrt{\det(\gamma_{ab})} \gamma^{cd} \gamma_{cd} - \partial_e \left(\sqrt{\det(\gamma_{ab})} \gamma^{cd} g_{\mu\lambda} \partial_c \delta^e_d \right) = 0 \tag{1.24}$$

By differentiating both the zeroth component of the EOM and (1.22) we obtain a differential equation for the evolution of ρ:

$$\frac{d\rho}{dt} = -H\rho\left(1+3v^2\right) \tag{1.25}$$

where v is the RMS velocity defined as

$$v^2 \equiv \left\langle \dot{\vec{x}}^2 \right\rangle = \frac{\int \dot{\vec{x}}^2 \epsilon d^2\sigma}{\int \epsilon d^2\sigma} \tag{1.26}$$

and the time derivative, in this case, is with respect to conformal time.

Furthermore we can perform a similar operation to the spatial components of (1.24) (i. e. $\lambda = i$) to obtain a differential equation for the evolution of v:

$$\frac{dv}{dt} = \left(1-v^2\right)\left(\frac{k_w}{L} - 3Hv\right) \tag{1.27}$$

where k_w is a curvature/momentum parameter, that is taken to be constant at a first approximation, and L is the correlation length:

$$L^{-1} \equiv \frac{a^2}{V} \int \epsilon \, d^2\sigma \tag{1.28}$$

To account for energy losses caused by intersections of walls and formation of closed sphere-like objects that collapse into themselves, we need to introduce a mechanism similar to what was done by Kibble for strings [21]:

$$\frac{d\rho_{loss}}{dt} = -c_w v \frac{\rho}{L} \tag{1.29}$$

where the *chopping* parameter c_w is taken to be constant. We can rewrite (1.25) introducing this energy loss term and representing it in terms of the correlation length ($L = \sigma_w/\rho$)

$$\frac{dL}{dt} = \left(1+3v^2\right) HL + c_w v \tag{1.30}$$

To obtain the relevant asymptotic scaling solutions one must neglect the effect of the energy density of the walls on the background (specifically, on the Friedmann equations). Even though the wall network energy will end up dominating, this is a good approximation in the context of the numerical simulations that will be carried out in this thesis. For a scale

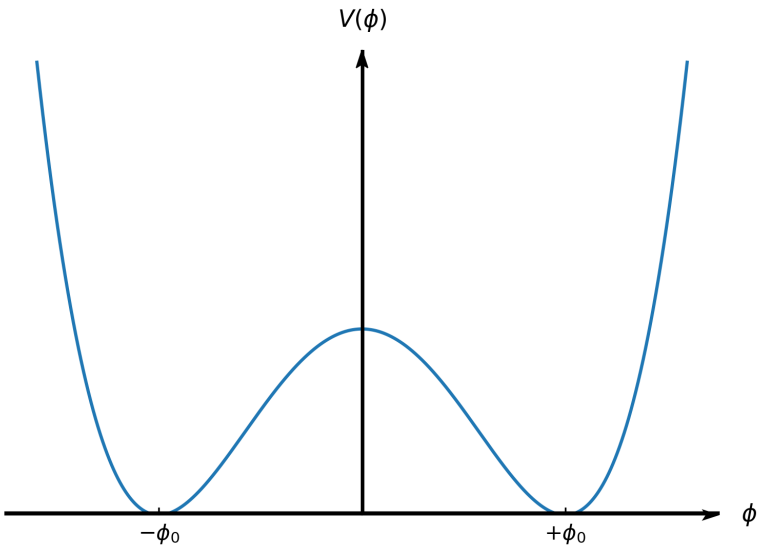

Figure 1.3: General shape of a double well ϕ^4 potential.

factor behaving as (1.9), the attractor solution for equations (1.30) and (1.27) corresponds to a linear scaling solution:

$$L = \sqrt{\frac{k_w\left(k_w + c_w\right)}{3\lambda\left(1-\lambda\right)}}\; t \tag{1.31}$$

$$v^2 = \frac{1-\lambda}{3\lambda}\frac{k_w}{k_w + c_w} \tag{1.32}$$

It's important to note that, since c_w and k_w are free parameters of the model, they need to be calibrated numerically using either bootstrapping techniques or more sophisticated methods such as MCMC [10].

1.2.3 The ϕ^4 potential

The prototypical model that is used to study the appearance and evolution of domain walls is described by (1.13) with a double-well potential of the form

$$V\left(\phi\right) = V_0\left(1 - \frac{\phi^2}{\phi_0^2}\right)^2 \tag{1.33}$$

Here, ϕ_0 is the potential energy minimum and V_0 is the height of the potential barrier and has the general shape represented in figure 1.3. This model has been extensively studied using both analytical and numerical approaches since it emerges naturally from current field

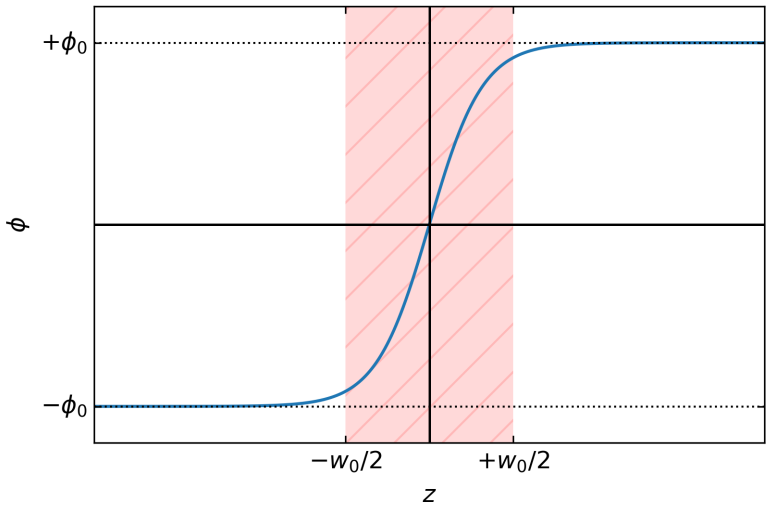

Figure 1.4: Shape of a planar wall at rest with a localized kink at $z = 0$ and a thickness of w_0 that interpolates between the two vacua localized at $\phi = \pm\phi_0$.

theory models. It can be shown that, for this case, equation (1.15) has the exact solution for an adiabatically static Universe

$$\phi(z) = \phi_0 \tanh\left(\frac{\sqrt{2V_0}}{\phi_0} z\right) \tag{1.34}$$

which corresponds to a planar wall at rest with a localized kink centered at $z = 0$.

By identifying its thickness to be

$$w_0 \equiv \frac{\pi\phi_0}{\sqrt{2V_0}} \tag{1.35}$$

we can rewrite (1.34) as

$$\phi(z) = \phi_0 \tanh\left(\frac{\pi}{w_0} z\right) \tag{1.36}$$

which is represented in figure 1.4.

Numerically (and for consistency throughout this thesis), we will want to calculate V_0 from a fixed value of the wall density w_0 so we can simply rearrange (1.35) to give us

$$V_0 = \frac{\pi^2\phi_0^2}{2w_0^2} \tag{1.37}$$

Furthermore, it can be shown that its surface tension is

$$\sigma = \frac{8}{3}\phi_0\sqrt{V_0} \tag{1.38}$$

and that this surface tension in the two tangential directions is also equal to σ_w.

Chapter 2

Numerical Approach

2.1 The PRS algorithm

This thesis will closely follow the method developed by Press, Ryden & Spergel [32].

A consequence of evolving equation equation (1.17) is that the wall thickness w_0 will decrease as a^{-1}. This creates a big problem when computing this model since, for later times, we lose resolution on the wall and can easily encounter energy losses related to numerical limitations. The PRS method solves this issue by introducing a new equation of motion that preserves the dynamics of (1.17) but maintains a constant comoving thickness for the walls. To do this, one first considers the general equation

$$\frac{\partial^2\phi}{\partial\eta^2}+\alpha\left(\frac{d\ln a}{d\ln\eta}\right)\frac{\partial\phi}{\partial\eta}-\nabla^2\phi=-a^\beta\frac{\partial V}{\partial\phi} \tag{2.1}$$

where α and β are constants. It's easy to see that equation (1.17) is the particular case where $\alpha=\beta=2$.

We can guarantee constant comoving wall thickness by removing the dependency on a in the right-hand side of the equation i.e. setting $\beta=0$. This however, may change the large scale dynamics of the system so we will also need to adjust α in order to preserve them, namely the rate at which the Hubble damping localizes ϕ into ϕ_0 and the momentum conservation law for how walls slow down in the Hubble flow. These are, respectively, determined by equations (2.2) and (2.3).

$$\langle\phi-\phi_0\rangle_{\rm rms}\propto a^{-\alpha/2-\beta/4} \tag{2.2}$$

$$\gamma v\propto a^{-\alpha-\beta/2} \tag{2.3}$$

A fortunate result is that setting $\alpha=3$ and $\beta=0$ in these equations gives us the same dynamics as in the original system but with the benefit of maintaining a constant comoving

wall thickness. By using this choice of parameters we obtain the final EOM that will be used to evolve the field

$$\frac{\partial^2\phi}{\partial\eta^2} + 3\left(\frac{d\ln a}{d\ln\eta}\right)\frac{\partial\phi}{\partial\eta} - \nabla^2\phi = -\frac{\partial V}{\partial\phi} \tag{2.4}$$

2.1.1 Discretization of the theory

The method used to discretize (2.4) is fairly standard. A simple finite differences scheme with a 7-point stencil was used to compute the 3-dimensional Laplace operator:

$$\left(\nabla^2\phi\right)_{ijk} \equiv \phi_{i+1,j,k} + \phi_{i-1,j,k} + \phi_{i,j+1,k} + \phi_{i,j-1,k} + \phi_{i,j,k+1} + \phi_{i,j,k-1} - 6\phi_{i,j,k} \tag{2.5}$$

For the time derivatives we used a staggered leapfrog finite differences scheme for the second-order term and Crank-Nicolson for the first-order term:

$$\dot{\phi}^{n+1/2}_{ijk} = \frac{(1-\delta)\,\dot{\phi}^{n-1/2}_{ijk} + \Delta\eta\left(\nabla^2\phi^n_{ijk} - \partial V/\partial\phi^n_{ijk}\right)}{1+\delta} \tag{2.6}$$

Here, $\dot{\phi} \equiv \partial\phi/\partial\eta$, $\Delta\eta$ is the discrete time step and the damping term δ is given by the expression

$$\delta \equiv \frac{1}{2}\alpha\frac{\Delta\eta}{\eta}\frac{d\ln a}{d\ln\eta} \tag{2.7}$$

By using a central difference scheme to compute $\dot{\phi}^{n+1/2}$ it's easy to realize that the evolution of the field is simply given by

$$\phi^{n+1}_{ijk} = \phi^n_{ijk} + \Delta\eta\dot{\phi}^{n+1/2}_{ijk} \tag{2.8}$$

2.2 Code implementation

The highly parallel nature of steps (2.5), (2.6) and (2.8) makes this algorithm a prime candidate for GPGPU implementation. This was firstly done by Correia and Martins [9] using Open Computing Language (OpenCL) 1.2 as specified by the Khronos Consortium [29] which allowed us to more efficiently run several simulations on a single machine.

The machine used for testing was equipped with a NVIDIA Quadro P5000 with 2560 CUDA cores clocked at $1607MHz$. It also packed $16GB$ of total video memory clocked at $1126MHz$.

The first relevant quantity that we wish to measure is the wall density, which is simply given by

$$\rho_w = \frac{A}{V} \tag{2.9}$$

where A is the comoving area of the wall and V is the volume of the box and is related to the correlation length as discussed in section 1.2.2. For this, we used the value of $\phi(\vec{x})$ on each point of the grid to determine if it was located at a maximum of $V(\phi)$ within a certain margin $\delta\phi$ and divide it by the total number of points in the grid. The other important quantity to measure is the wall RMS velocity, more specifically γv (where γ is the the Lorentz factor) which was done in accordance to the method described in [3] where this quantity is shown to be given by

$$\left\langle \gamma^2 v^2 \right\rangle = \sum \frac{\dot{\phi}^2}{2V(\phi)} \tag{2.10}$$

and the sum is computed only over the points in the field that are located at a maximum of $V(\phi)$.

The initial state of the field ϕ was assumed to be a randomly distributed variable between $-\phi_0$ and $+\phi_0$ with $\partial\phi/\partial\eta = 0$. This leads to large energy gradients in the initial time steps of the simulations that need some time to dissipate. In some cases on this thesis we had to introduce a cooling mechanism where we temporary allowed the field to evolve without expansion to soften these gradients.

All simulations start at a conformal time $\eta = 1$ and evolve in time steps of $\Delta\eta = 0.25$ until a conformal time equal to half the box size. This upper bound is set to prevent unwanted interactions of the field as a result of using periodic boundary conditions. It's also worth mentioning that, when the cooling mechanism is introduced (for $\eta < 1$), the time step needs to be much finer to prevent numerical errors, specifically we chose $\Delta\eta_{cooling} = \Delta\eta/30$.

All the results presented were averaged from 10 separate runs with 10 different seeds in the initial conditions (for consistency, the same 10 different seeds were used in every chapter) and a box size of 2048^2.

To keep the results consistent throughout all simulations and previous works, we also decided to set $\phi_0 = 1$ and $w_0 = 5$ when computing its evolution.

2.3 Consistency tests for the ϕ^4 potential case

To test the validity of the code we first implemented it for the simple case of the double well potential discussed in section 1.2.3. By using the definition for V_0 in (1.37) along with the previously mentioned values for ϕ_0 and w_0, equation (1.33) becomes:

$$V(\phi) = \frac{\pi^2}{50}\left(1-\phi^2\right)^2 \tag{2.11}$$

For this test we decided to use three different expansion rates: a radiation dominated Universe with $\lambda = 1/2$, a matter dominated Universe with $\lambda = 2/3$ and an accelerated expansion with $\lambda = 4/5$. We chose to represent in figure 2.1 simulations for radiation and matter dominated Universes for two distinct time steps. Plotted in figures 2.2 and 2.3 are the evolution of the wall density and velocity, respectively, using our method.

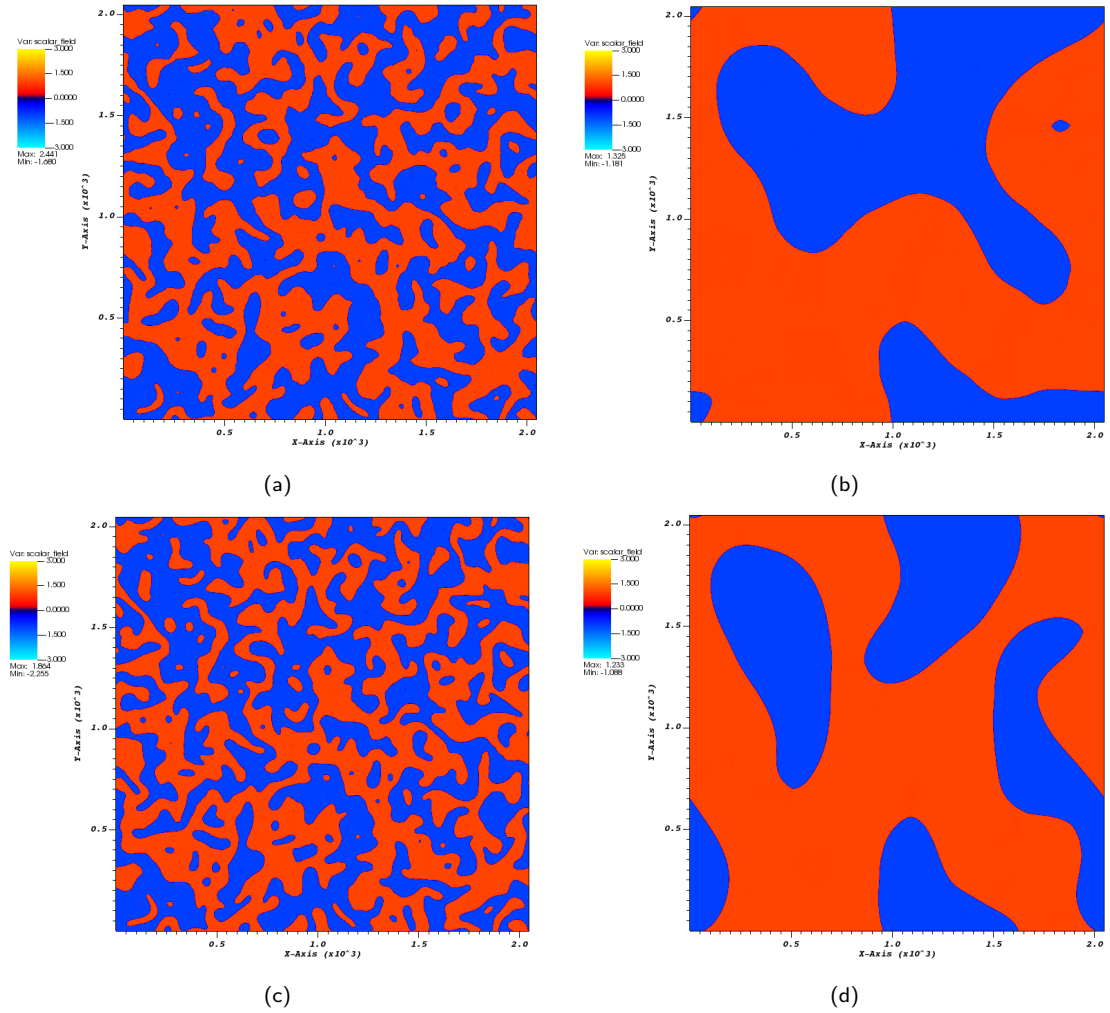

Figure 2.1: Pictures of a domain wall network in a quartic potential and a 2048^2 grid evolved using the method described in this chapter for $\lambda = 1/2$ (2.1a and 2.1b) and $\lambda = 2/3$ (2.1c and 2.1d). The color represents the value of the field ϕ. Snapshots were taken for conformal times $\eta = 101$ (2.1a and 2.1c) and $\eta = 751$ (2.1b and 2.1d).

It shows that, after an initial period of about $\eta = 20$, the evolution assumes a stable behavior similar to the one predicted by the VOS model. In order to quantify this relationship we looked for the best fit to the power laws

$$\rho_w \propto \eta^{\mu} \tag{2.12}$$

$$\gamma v \propto \eta^{\nu} \tag{2.13}$$

For a scale invariant behavior, we should expect $\mu = -1$ and $\nu = 0$. There needs to be special care to only fit the data in the relevant dynamic range which, in this case, we chose to be $\eta > 21$. We also calculated the asymptotic values of $(\rho_w \eta)^{-1}$ and γv on the later stages of evolution where we assumed to have achieved scaling. These quantities are directly used to calculate the parameters c_w and k_w in the analytical model.

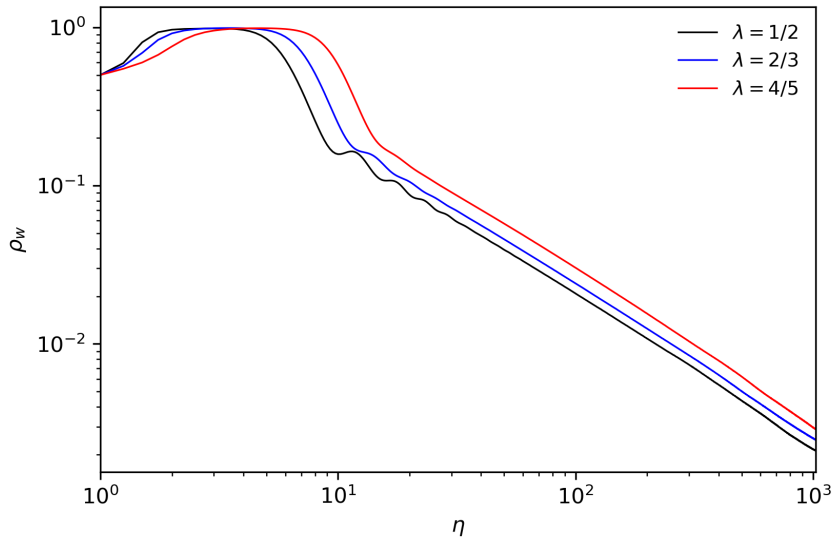

Figure 2.2: Evolution of the domain wall density in a ϕ^4 potential as a function of conformal time for a box size of 2048^2 and three different expansion rates. The plotted curves are averaged over 10 different simulations with different random initial conditions, identical for each value of λ.

Table 2.1 shows that the values we obtained are consistent with the analytical model and with the work done previously by Leite and Martins [23] who used an independent (CPU based) version of the code and ran it for exponents identical to ours.

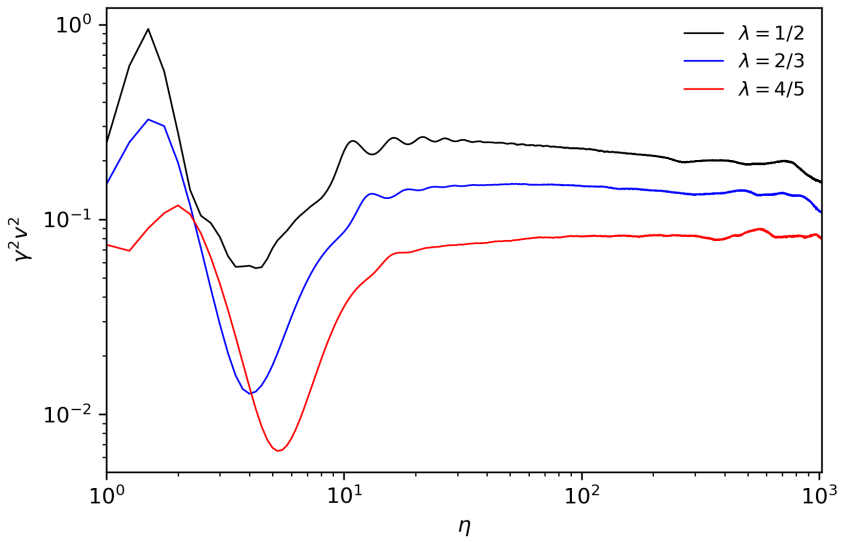

Figure 2.3: Evolution of the domain wall velocity ($\gamma^2 v^2$) in a ϕ^4 potential as a function of conformal time for a box size of 2048^2 and three different expansion rates. The plotted curves are averaged over 10 different simulations with different random initial conditions, identical for each value of λ.

Table 2.1: Comparison of the values for the exponents μ and ν calculated for three different expansion rates where the field is constrained by a ϕ^4 potential between our work and Leite and Martins (2011). Our values were taken by averaging over 10 simulations and fitting the data in the range $\eta = [21, 1024]$. The fourth and fifth column show the asymptotic values for $(\rho_w \eta)^{-1}$ and γv which in turn are related to the macroscopic values of the VOS model. Values in parentheses refer to the box size used in each case.

	λ	μ	ν	$(\rho_w \eta)^{-1}$	γv
Rosa (2048^2)	$1/2$	-0.93 ± 0.03	-0.06 ± 0.02	0.49	0.41
Rosa (2048^2)	$2/3$	-0.94 ± 0.02	-0.03 ± 0.03	0.42	0.35
Rosa (2048^2)	$4/5$	-0.94 ± 0.02	-0.00 ± 0.04	0.35	0.28
Leite & Martins (512^3)	$1/2$	-0.99 ± 0.05	-0.0001 ± 0.0002	0.60	0.46
Leite & Martins (512^3)	$2/3$	-0.97 ± 0.04	-0.0000 ± 0.0001	0.54	0.37
Leite & Martins (512^3)	$4/5$	-0.96 ± 0.03	0.00001 ± 0.00005	0.50	0.29

Chapter 3

Sine-Gordon Potential

3.1 Introduction

Another potential shape that emerges from specific symmetry breaking mechanisms such as the in the schizon models [16] is the Sine-Gordon potential:

$$V(\phi) = V_0^{\mathrm{SG}} \left[1 + \cos\left(\pi \frac{\phi}{\phi_0}\right)\right] \tag{3.1}$$

which has periodic minima at $(2n+1)\,\phi_0$ for any integer n, as shown in figure 3.1.

For consistency through this work it is important to relate V_0 with the wall thickness w_o which is a fixed value in our simulations. To guarantee that the field has the same dynamics in the vacuum as in ϕ^4 we must choose a value of V_0 that preserves the local curvature at the minima that are common to both models. To do this, we simply calculate the second derivative of both the ϕ^4 (1.33) and Sine-Gordon (3.1) potentials:

$$\left.\frac{d^2 V_{\phi^4}}{d\phi^2}\right|_{\phi=\pm\phi_0} = \frac{8V_0}{\phi_0^2} \qquad , \qquad \left.\frac{d^2 V_{\mathrm{SG}}}{d\phi^2}\right|_{\phi=\pm\phi_0} = \frac{\pi^2 V_0^{\mathrm{SG}}}{\phi_0^2} \tag{3.2}$$

By imposing that they must have the same local curvature in the vacua, we get a relationship between V_0 and V_0^{SG}:

$$V_0^{\mathrm{SG}} = \frac{8}{\pi^2} V_0 \tag{3.3}$$

Using this relation and plugging the same values for ϕ_0 and w_0 as we used in the previous section, we can rewrite the potential (3.1) as

$$V(\phi) = \frac{4}{25}\left[1 + \cos(\pi\phi)\right] \tag{3.4}$$

This formulation ensures similar local field dynamics in the minima while at the same time having the same fixed wall thickness as in the ϕ^4 case.

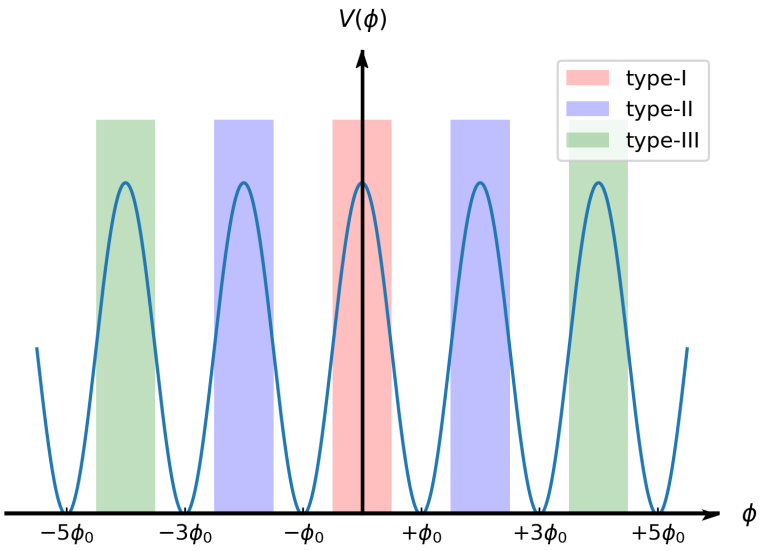

Figure 3.1: General shape of the Sine-Gordon potential and the different types of walls it can produce in each maxima.

3.2 Evolution of ρ and v

We used the same procedure as in the previous section to evaluate the evolution of domain walls emerging from this type of potential, specifically the wall separating the vaccua at $\pm\phi_0$. For consistency we chose to represent in figure 3.2 snapshots of the field for $\lambda = 1/2$ and $\lambda = 2/3$ and used the same initial conditions as in 2.1. Since the initial conditions are identical to the ones used in the ϕ^4 model, in the initial time steps only type-I walls can exist and other types that form at later times are solely a consequence of the dynamics of the model.

Since the field can explore several minima, it will naturally do so in the initial time steps where it has enough energy. Figure 3.4 shows us how these domains emerge in the simulation and cause the formation of different types of walls. The data for the density and velocity of each type of wall is plotted in figure 3.3. From 3.3c and 3.3e we can easily see that higher expansion rates have less type-II and type-III walls. This is an expected result since the smaller Hubble damping gives the opportunity for more areas to cross to other minima. We also found that, given the initial conditions, no walls form between the third and fourth minima for the expansion rates evaluated. The density plot for type-III walls also suggests that these defects are very sparse and short-lived given these conditions.

More conclusions can be drawn by analysing the ratio of density and velocity between the "outer" walls and type-I. This can give us a clearer picture on how their dynamics diverge from one another. We only plotted the ratios between type-II and type-I in figure 3.5 because data for the other walls was too noisy. Nevertheless figure 3.5a clearly shows that type-II walls also decay slightly faster then type-I. Figure 3.5b on the other hand suggests that the velocity of type-II walls has the same behaviour as velocity of type-I walls. Despite having the same order

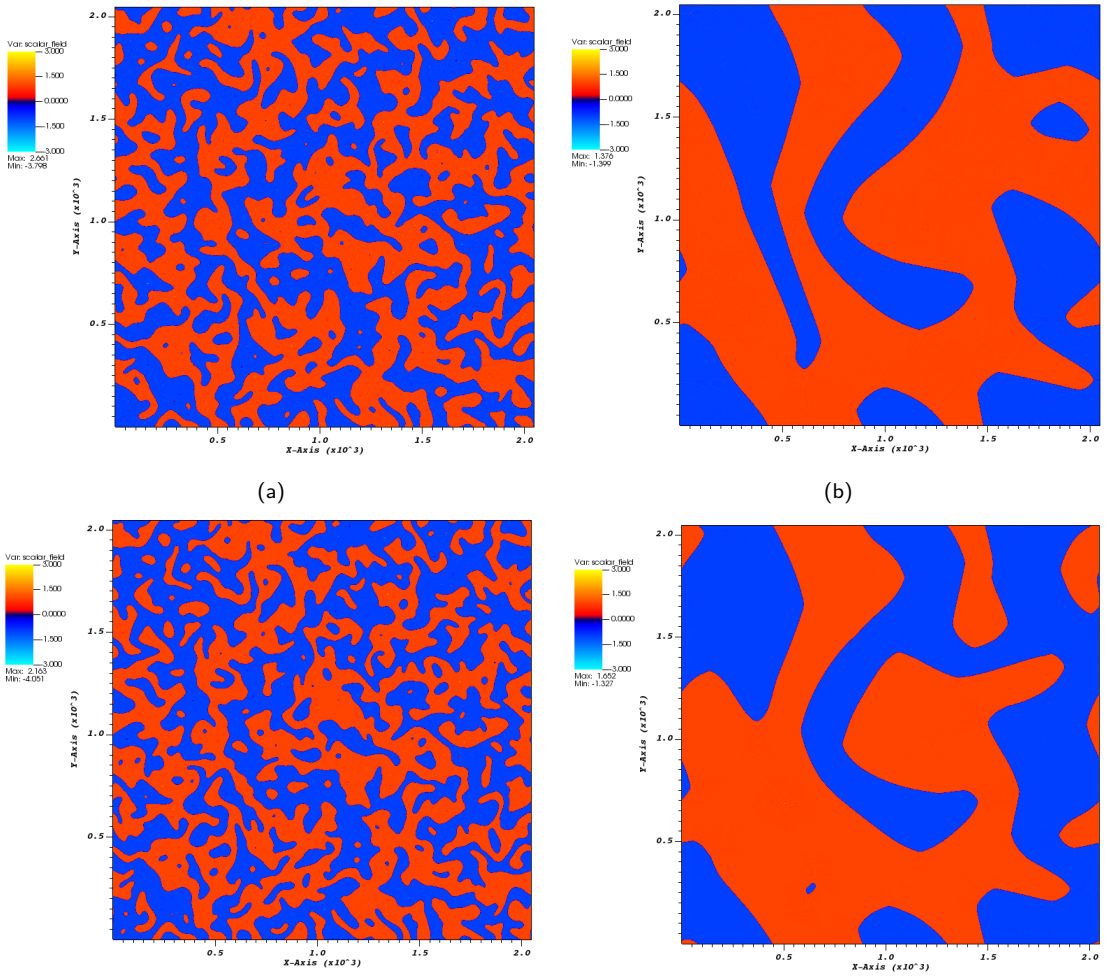

Figure 3.2: Pictures of a domain wall network in a Sine-Gordon potential and a 2048^2 grid evolved using the method described in chapter 2 with $\lambda = 1/2$ (3.2a and 3.2b) and $\lambda = 2/3$ (3.2c and 3.2d). The color represents the value of the field ϕ. Snapshots were taken for conformal times $\eta = 101$ (3.2a and 3.2c) and $\eta = 751$ (3.2b and 3.2d).

of magnitude it's also clear that, the faster the expansion rate is, the faster type-II walls move, more specifically the ratio for the velocities $\left((\gamma v)^2_{II} \,/\, (\gamma v)^2_{I}\right)$ is approximately 1.95 for $\lambda = 1/2$, 2.34 for $\lambda = 2/3$ and 3.49 for $\lambda = 4/5$. This again, is an expected result since the field needs more energy to overcome the potential which means that, when it does, it naturally has more kinetic energy.

Similarly to what was done in the previous section, we tried to model the data to the semi-analytical VOS model. By fitting the data from type-I walls to (2.12) and (2.13) we obtained the values presented in table 3.1.

As we can see, they significantly deviate from the values for a scaling solution of the VOS model. In the case of ϕ^4 it is known that these values might change depending on the size and dimension of the box used to perform the simulations [23]. Whether this deviation is a consequence of this or if it serves as a clue that the VOS model needs to be further refined is still an open problem.

Table 3.1: Values for the exponents μ and ν calculated for three different expansion rates for type-I and type-II walls in a Sine-Gordon potential and a box size of 2048^2. Each value was taken by averaging over 10 simulations and fitting the data in the range $\eta = [26, 1024]$ for type-I and $\eta = [31, 1024]$ for type-II walls. The fifth and sixth column show the asymptotic values for $(\rho_w \eta)^{-1}$ (which couldn't be computed for type-II walls since ρ_w goes asymptotically to $\rho_w = 0$ given our resolution) and γv which in turn are related to the macroscopic values of the VOS model.

Wall type	λ	μ	ν	$(\rho_w \eta)^{-1}$	γv
Type-I	$1/2$	-0.84 ± 0.02	-0.21 ± 0.02	0.40	0.30
Type-I	$2/3$	-0.85 ± 0.01	-0.18 ± 0.02	0.37	0.27
Type-I	$4/5$	-0.87 ± 0.01	-0.14 ± 0.02	0.33	0.25
Type-II	$1/2$	-1.45 ± 0.04	-0.04 ± 0.01	-	0.50
Type-II	$2/3$	-1.38 ± 0.06	-0.06 ± 0.01	-	0.52
Type-II	$4/5$	-1.54 ± 0.05	-0.07 ± 0.01	-	0.52

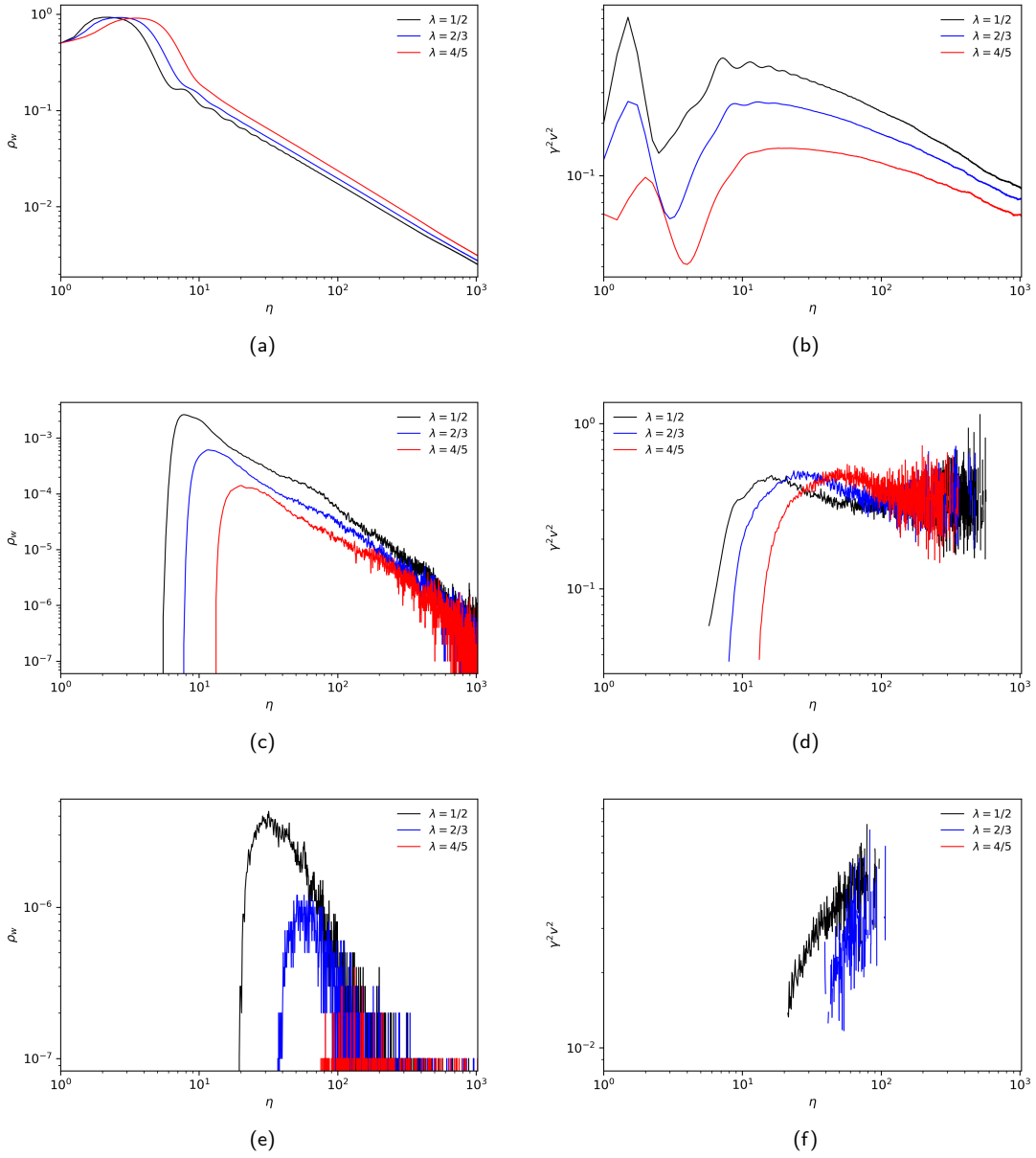

Figure 3.3: Evolution of the density and velocity ($\gamma^2 v^2$) of different types of domain walls that form in a Sine-Gordon potential as a function of conformal time for a box size of 2048^2. The plots 3.3a and 3.3b correspond to the type-I walls formed between the two central minima between $\phi = \pm 1$, the plots 3.3c and 3.3d correspond to the type-II walls that form between the the central minima and the following ones at $\phi = \pm 3$ and the bottom plots, 3.3e and 3.3f, correspond to the type-III walls that form between the minima at $\phi = \pm 3$ and the ones at $\phi = \pm 5$.

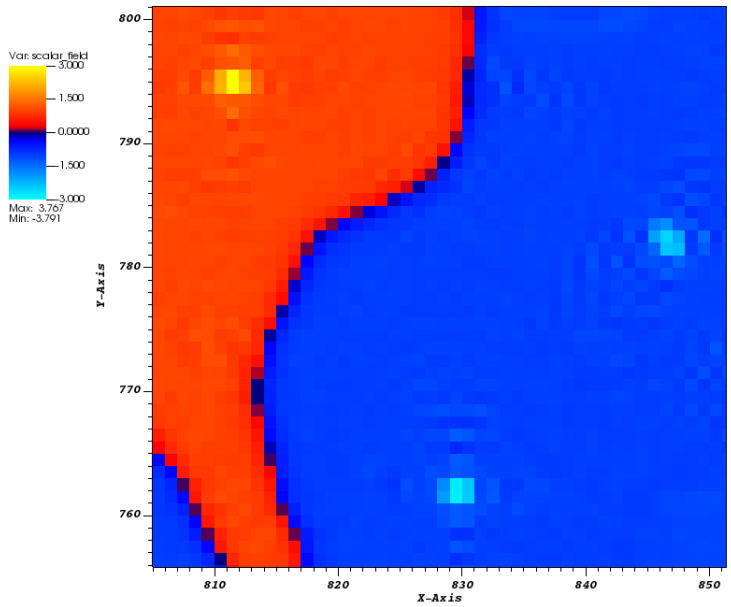

Figure 3.4: Picture of the field that details the emergence of domains outside the initial conditions in a Sine-Gordon potential giving rise to type-II walls. The color represents the value of the field ϕ. This snapshot was taken from a simulation using the method detailed in chapter 2 for a box size of 2048^2 and $\lambda = 1/2$ at conformal time $\eta = 26$.

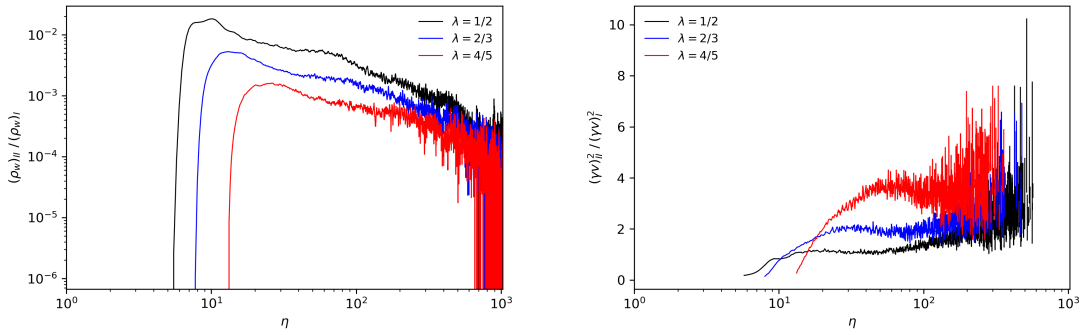

(a) (b)

Figure 3.5: Ratios between density and velocity of type-I and type-II walls that form in a Sine-Gordon potential. It was used the same data as in figure 3.3.

Chapter 4

ϕ^6 Potential

4.1 Introduction

In this section we aim to analyse the cosmological evolution of a scalar field when constrained by a triple well potential defined by

$$V(\phi) = V_0 \frac{\phi^2}{\phi_0^2}\left(1 - \frac{\phi^2}{\phi_0^2}\right)^2 \tag{4.1}$$

which has minima located at $\phi = 0$ and $\phi = \pm\phi_0$ as shown in figure 4.1.

This type of potential has been studied extensively in the context of both condensed matter and high energy particle physics, most notably as a natural extension of the Ginzburg-Landau model (see for example [5, 4, 11, 13, 19, 2, 36, 24, 22]). In this thesis we will focus on how this potential behaves in an expanding Universe and its ability to form domain walls.

We will work on the ansatz that the wall thickness relates to V_0 in the same as in ϕ^4 defined in equation (1.37) since it preserves the same curvature at the side minima ($\phi = \pm\phi_0$). This can be validated by a similar analysis as it was done in the previous section where we calculated the second derivative of the potential in that minima. For our purposes, this means that we can rewrite (4.1) as

$$V(\phi) = \frac{\pi^2}{50}\phi^2\left(1 - \phi^2\right)^2 \tag{4.2}$$

where we used the same values for w_0 and ϕ_0 as in the previous sections.

4.2 Evolution of ρ and v

The same procedure as in the previous chapters was used to determine the evolution of the density and velocity for the walls, which were considered to be the points of the field between the middle minimum at $\phi = 0$ and the two side minima $\phi = \pm 1$. The results are shown in 4.2 and 4.3 and they clearly show that there is no defect formation in any of the expansion rates and that the area of points between the minima quickly falls to 0 in a time scale of $\eta < 8$.

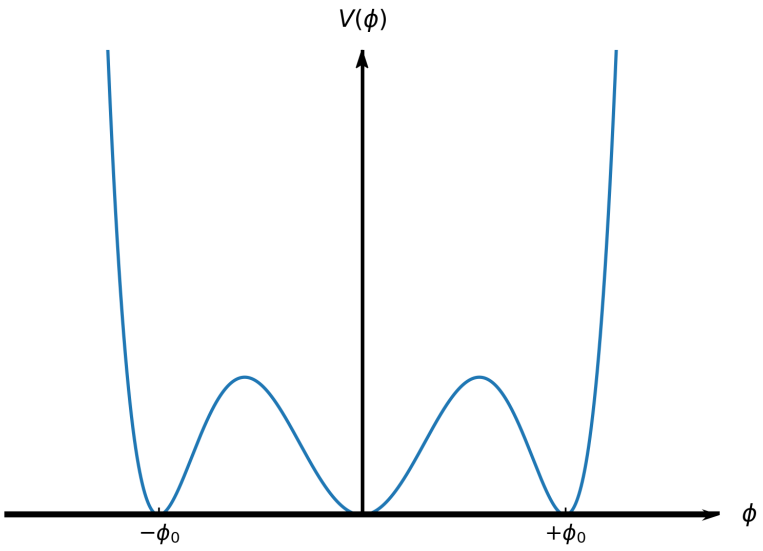

Figure 4.1: General shape of a triple well ϕ^6 potential.

4.3 Field Collapse

To better understand the mechanism behind this collapse we looked for the values that the field manifested. We concluded that the absence of walls was a consequence of the field quickly collapsing to $\phi = 0$ as figure 4.4 shows. This is also evident when we plot the density of points in this minimum as shown in figure 4.5.

We propose that this is a consequence of the damping caused by the expansion and the random symmetrical nature of the initial conditions. We tried to address the former by introducing a cooling mechanism as described in section 2.2. This proved to be ineffective in preventing the collapse. The latter might be curbed by introducing biased initial conditions such as in the analysis done by Correia et al. [7, 8] for the ϕ^4 case. We know of asymmetries that occur in nature, such as in the case of the open baryon asymmetry problem, so it could be interesting to investigate whether the introduction of biased initial conditions in a ϕ^6 potential could give rise to domain walls without the introduction of additional constrains in the potential itself.

4.4 Christ-Lee Potential

In this section we investigate the possibility of wall formation in a triple well potential by introducing a constraint in the potential making the central minimum metastable and try to extend this model to a pure ϕ^6 potential. For that purpose we compute the field in a Christ-Lee

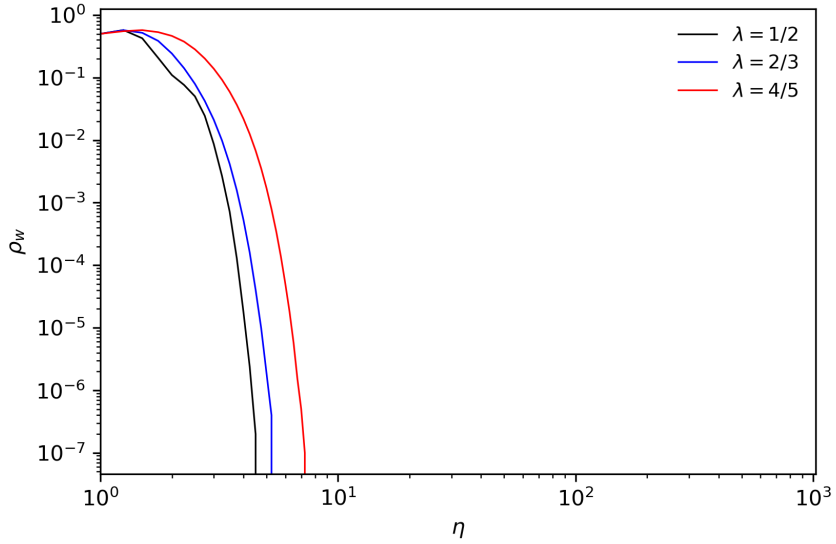

Figure 4.2: Evolution of the density of domain walls in a ϕ^6 potential as a function of conformal time for a box size of 2048^2 and three different expansion rates. The plotted curves are averaged over 10 different simulations with different random initial conditions, identical for each value of λ.

type potential [6] that has an aditional parameter ε which interpolates the potential between ϕ^4 (when $\varepsilon \to \infty$) and ϕ^6 (when $\varepsilon = 0$) and is given by

$$V(\phi) = V_0 \left(\frac{\phi^2/\phi_0^2 + \varepsilon^2}{1+\varepsilon^2} \right) \left(1 - \frac{\phi^2}{\phi_0^2} \right)^2 \tag{4.3}$$

The ability for this potential to replicate the scaling exponents μ and ν from section 2.3 for a sufficiently high $\varepsilon \geq 1$ is shown in table 4.1 and serves as an important consistency test by itself. This is furthermore validated by figure 4.7 which shows that the evolution of the network for $\varepsilon = 1$ has an indistinguishable behaviour from the quartic model. Nevertheless, when we look at the asymptotic values for the density we can see that they clearly deviate from the values we got in section 2.3, even though the asymptotic values for the velocity have remain consistent for $\varepsilon = 2$ and $\varepsilon = 4$. These values will be ultimately used together to calibrate the parameters of the VOS model, so this variation can have a significant impact in the analytical model and is likely caused by the different shape of the potential.

The Christ-Lee potential effectively creates a bias between the minima keeping the side minima fixed at $\phi = \pm\phi_0$ and varying the central minimum at $\phi = 0$. It can be seen that this minimum emerges only for values of $\varepsilon < 1/\sqrt{2}$ as shown in figure 4.6. An important quantity to take into consideration is the difference in potential between the central and the outer minima ΔV, which is simply given by

$$\Delta V = V_0 \frac{\varepsilon^2}{1+\varepsilon^2} \tag{4.4}$$

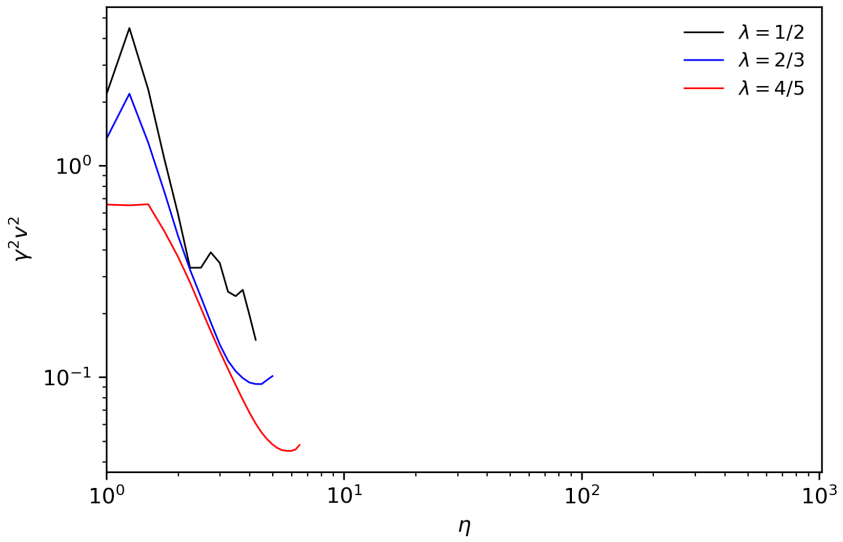

Figure 4.3: Evolution of the velocity ($\gamma^2 v^2$) of domain walls in a ϕ^6 potential as a function of conformal time for a box size of 2048^2 and three different expansion rates. The plotted curves are averaged over 10 different simulations with different random initial conditions, identical for each value of λ.

Another useful property is that the curvature of the side minima does not depend on ε and it's the same as in the the pure ϕ^6 case which makes it reasonable to use the same ansatz as in ϕ^6 where we took the wall thickness w_0 to be related to V_0 in the same way as in the simple ϕ^4 case. This means that (4.3) can be rewritten with these considerations and the same values for w_0 and ϕ_0 as

$$V(\phi) = \frac{\pi^2}{50}\left(\frac{\phi^2+\varepsilon^2}{1+\varepsilon^2}\right)\left(1-\phi^2\right)^2 \tag{4.5}$$

4.4.1 Stability analysis of the metastable vacuum

Our aim is to understand how the formation of walls depends on ΔV when dealing with a symmetric triple well potential so several simulations were made for the same initial conditions but for different values of ε. More specifically, we looked at how the density of points in the central minimum evolved over the simulations. If we expect walls to form, this value should drop after an initial stabilization period.

The result of these simulations is plotted in figure 4.8 for the case of a radiation dominated Universe. We used a threshold of $\rho < 2/3$ to estimate the time at which the vacuum decayed. Doing this allowed us to plot the dependence of this vacuum decay time to the parameter ε. Figure 4.9 shows us a clear ceiling for the formation of walls at $\varepsilon = 1/\sqrt{2}$ coinciding with the value for which the potential becomes a double well.

We concluded that this was a consequence of the high gradients of the field in the initial time steps of the simulation canceling each other as the increase of $a(\tau)$ acts as a damping

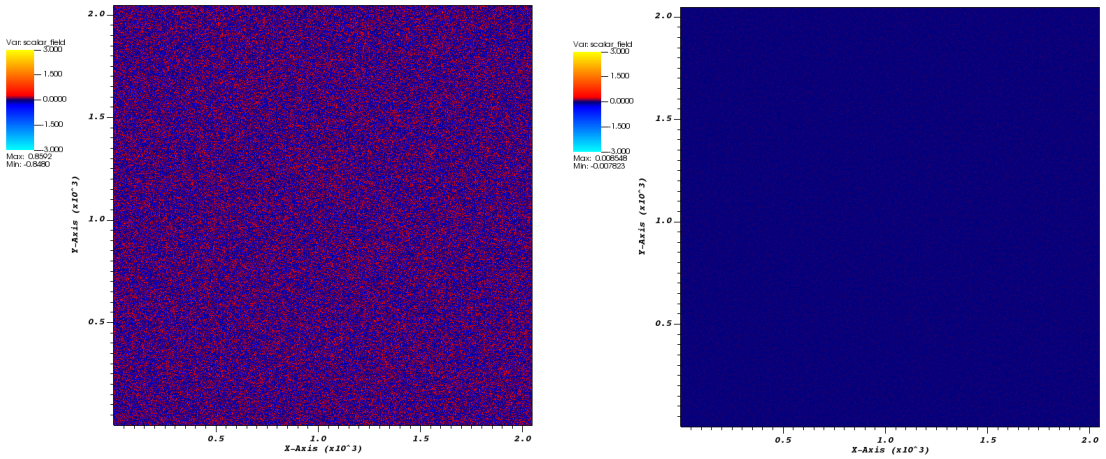

(a) (b)

Figure 4.4: Pictures depicting the field collapsing in a ϕ^6 potential and a 2048^2 grid evolved using the method described in chapter 2 for $\lambda = 1/2$. The color represents the value of the field ϕ. Snapshots were taken for conformal times $\eta = 2$ (4.4a) and $\eta = 51$ (4.4b).

mechanism. In order to overcome this issue we introduced the cooling mechanism referred in section 2.2 in our simulations. This, in fact, proved to facilitate the vacuum decay for $\varepsilon < 1/\sqrt{2}$.

We showed that the possibility of decay and the decay time of such a potential depends on the difference between the minima ΔV, the expansion rate λ and the initial cooling time of the field η_{cooling}. This threshold is plotted in figure 4.10 for a radiation dominated Universe and a matter dominated Universe. We can see that, for both cases, this threshold goes to $\Delta V = 1/3$ when we have no cooling (corresponding to $\varepsilon = 1/\sqrt{2}$) and seems to approach $\Delta V = 0$ as we increase the cooling time. This suggests that, regardless of the time we let the system cool before expansion, given symmetric initial conditions, a pure ϕ^6 potential will never give rise to domain walls. The main difference between the different values of λ seems to be "slope" of the threshold curve where, in a slower expansion, ΔV approaches 0 quicker when increasing the cooling time.

We can look at figure 4.11 to see how this vacuum decay occurs through bubble nucleation from the false vacuum. Attempts to model this decay followed the work done by Hindmarsh [17] where a potential bias between two minima is expected to follow a behaviour of the shape

$$\rho \propto \eta^{-1} \exp\left[-\kappa \left(\Delta V \eta\right)^n\right] \tag{4.6}$$

with κ being a normalization constant and n the number of spatial dimensions ($n = 2$ in our case). This approach, however, was proven to fail in this particular case due to the existence of global symmetry of the potential or by merely the existence of three minima. Both of these hypotheses should be explored, and a precise analytical (or even empirical) model for the curves shown in 4.10 would prove very useful for studying the domains for wall formation and fine tune cosmological constrains.

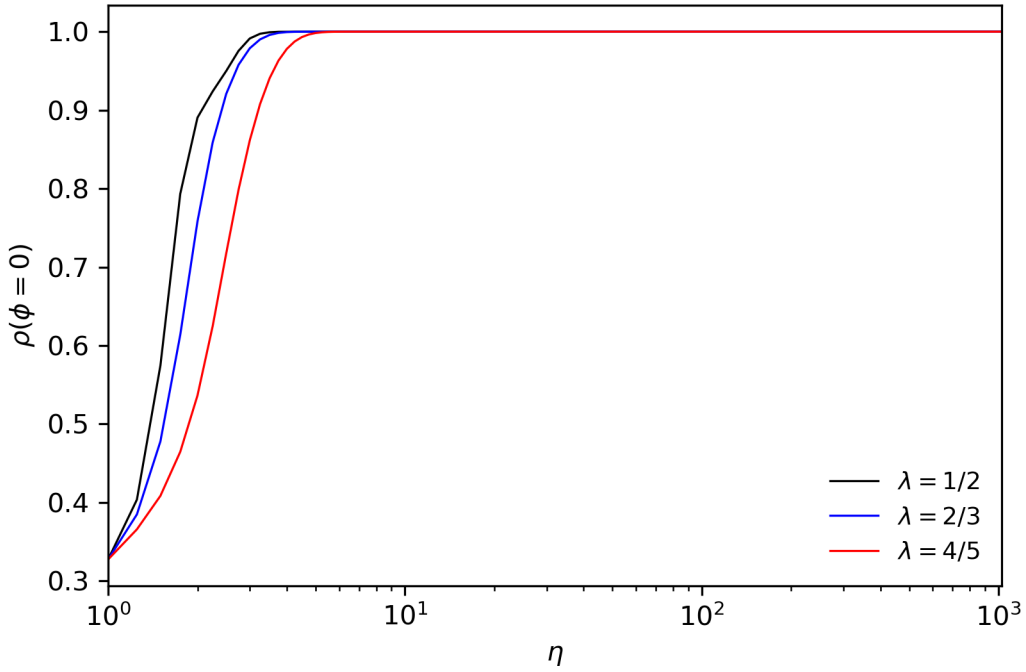

Figure 4.5: Evolution of the density of the field ϕ located at the central minimum ($\phi = 0 \pm 0.4$) in a ϕ^6 potential as a function of conformal time for a box size of 2048^2 and three different expansion rates. The plotted curves are averaged over 10 different simulations with different random initial conditions, identical for each value of λ.

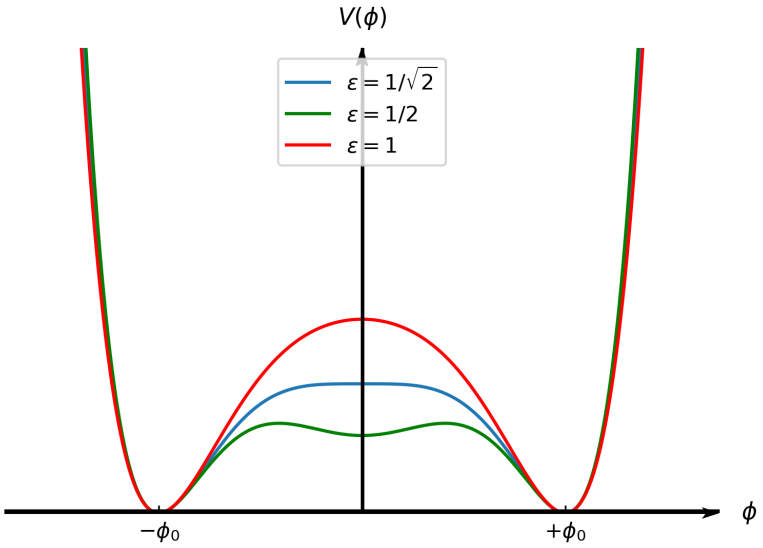

Figure 4.6: General shape of the Christ-Lee Potential potential that interpolates between a double well and a triple well for different values of ε.

Table 4.1: Values for the exponents μ and ν calculated for three different expansion rates in a box size of 2048^2 where the field is constrained by a Christ-Lee potential parameterized by different values of ε. Each value was taken by averaging over 10 simulations and fitting the data in the range $\eta = [31, 1024]$. The fifth and sixth column show the asymptotic values for $(\rho_w \eta)^{-1}$ and γv which in turn are related to the macroscopic values of the VOS model.

ε	λ	μ	ν	$(\rho_w \eta)^{-1}$	γv
1	1/2	-0.93 ± 0.02	-0.05 ± 0.05	0.41	0.33
1	2/3	-0.95 ± 0.02	-0.02 ± 0.04	0.37	0.27
1	4/5	-0.94 ± 0.01	-0.01 ± 0.05	0.30	0.21
2	1/2	-0.94 ± 0.03	-0.02 ± 0.04	0.57	0.43
2	2/3	-0.94 ± 0.02	-0.02 ± 0.04	0.46	0.34
2	4/5	-0.95 ± 0.01	-0.00 ± 0.05	0.37	0.26
4	1/2	-0.95 ± 0.03	-0.06 ± 0.02	0.62	0.41
4	2/3	-0.96 ± 0.03	-0.03 ± 0.03	0.54	0.35
4	4/5	-0.96 ± 0.02	$+0.03 \pm 0.04$	0.44	0.29

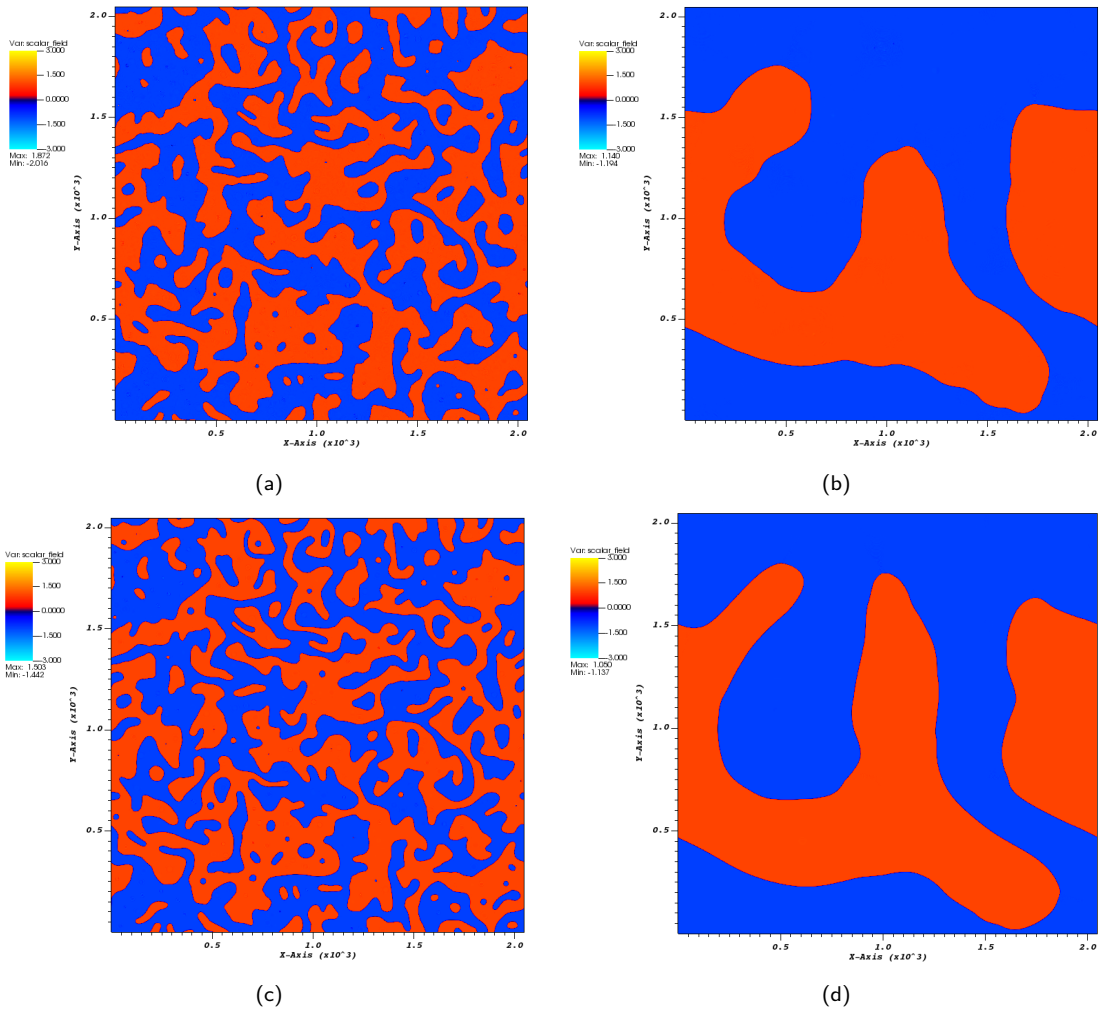

Figure 4.7: Pictures of a domain wall network in a Christ-Lee potential and a 2048^2 grid evolved using the method described in chapter 2 for $\lambda = 1/2$ (4.11a and 4.11b) and $\lambda = 2/3$ (4.11c and 4.11d) and $\varepsilon = 1$. The color represents the value of the field ϕ. Snapshots were taken for conformal times $\eta = 101$ (4.11a and 4.11c) and $\eta = 751$ (4.11b and 4.11d).

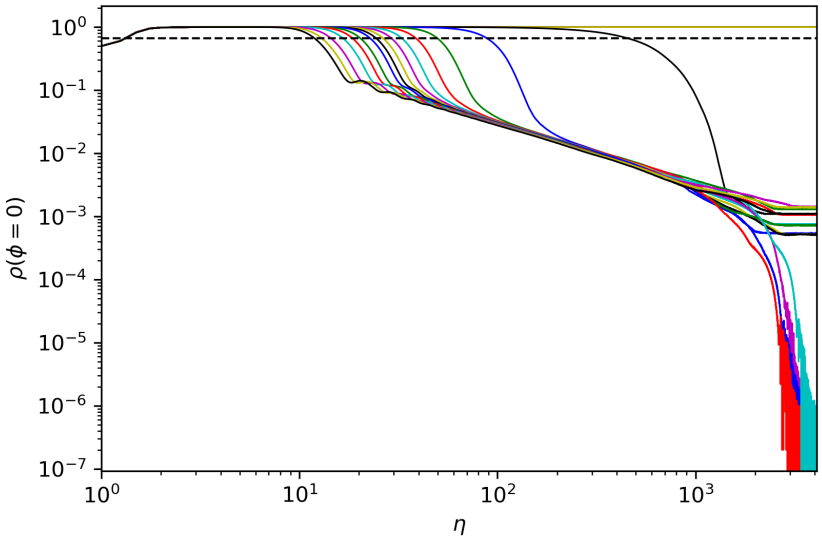

Figure 4.8: Evolution of the density of the field ϕ located at the the central minimum ($\phi = 0 \pm 0.4$) in a Christ-Lee potential as a function of conformal time for a radiation dominated Universe ($\lambda = 1/2$). Different colored lines represent different values of ε. This data was taken from averaging 10 simulations for each ε for the same initial conditions and a box size of 2048^2. The dashed line at $\rho = 2/3$ represents the threshold used to calculate vacuum decay.

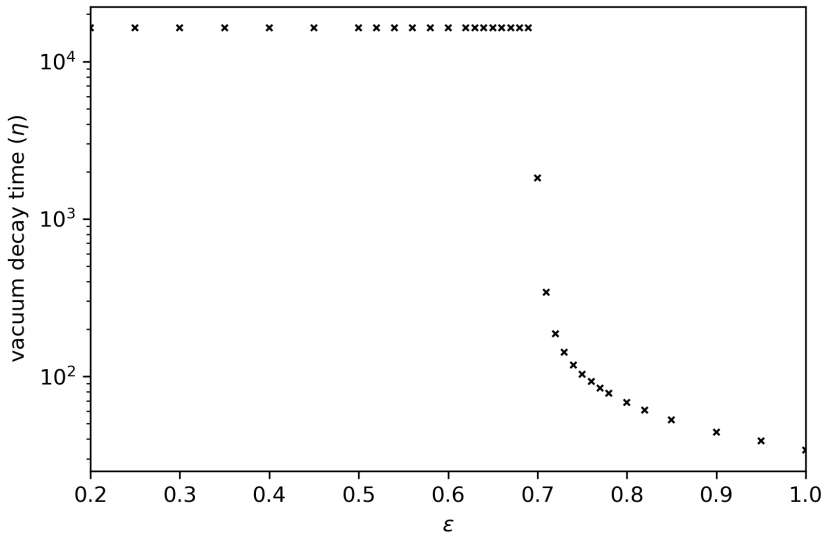

Figure 4.9: Dependence of the vacuum decay on ε taken from the data of figure 4.8 using $\rho < 2/3$ as the condition for decay.

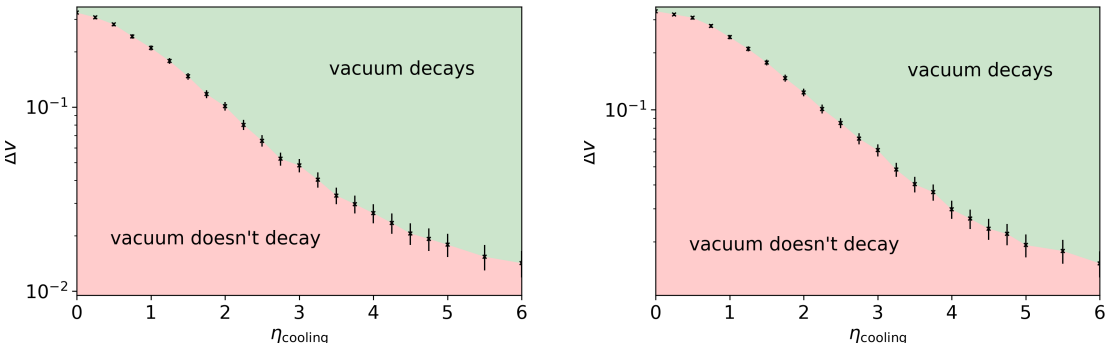

Figure 4.10: Dependency of vacuum decay in a Christ-Lee potential in terms of the initial cooling time of the field (η_{cooling}) and ΔV for $\lambda = 1/2$ (4.10a) and $\lambda = 2/3$ (4.10b). This data was averaged over 10 simulations for each value of ε and λ in a box size of 2048^2 and the decay was considered to occur when $\rho(\phi = 0 \pm 0.4) < 2/3$.

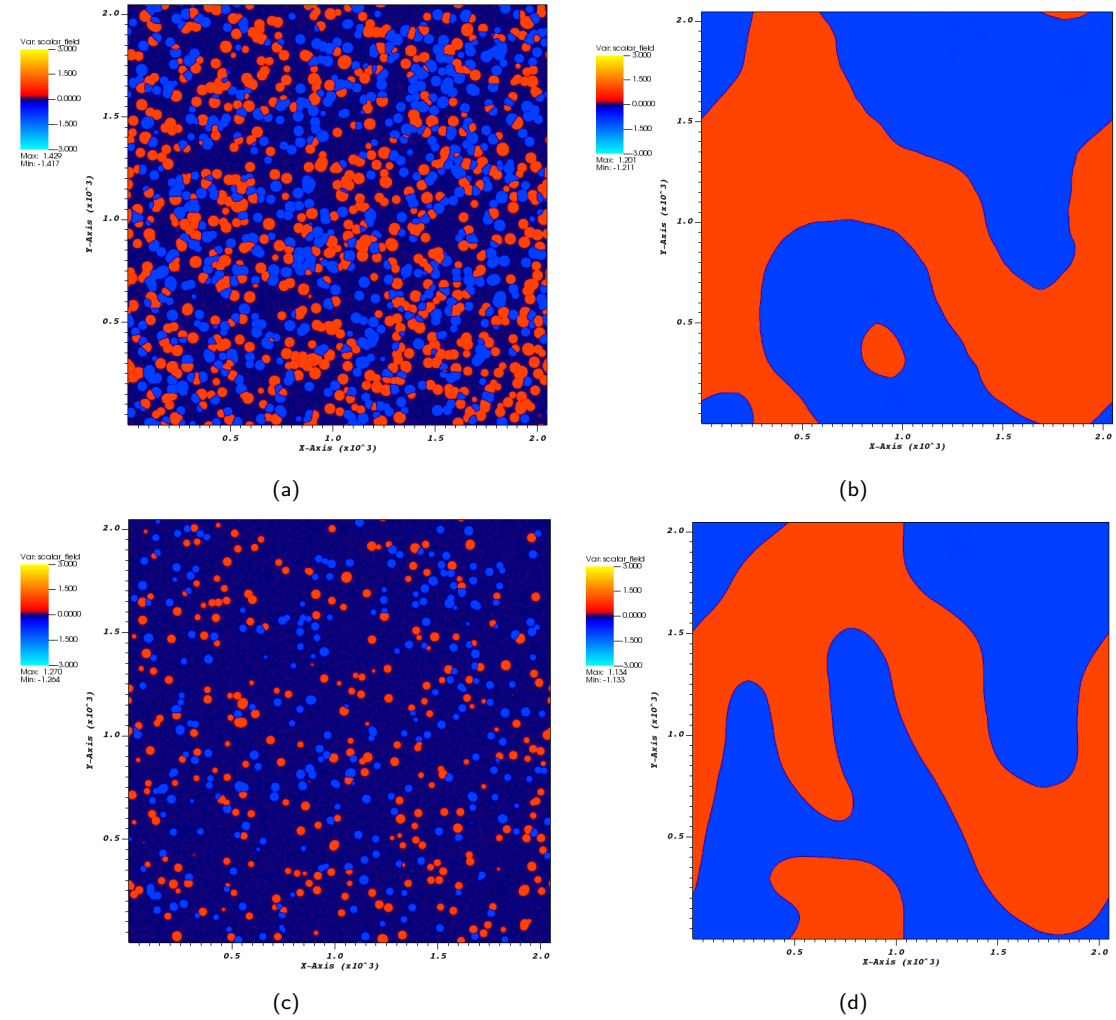

Figure 4.11: Pictures of a domain wall network in a Christ-Lee potential and a 2048^2 grid evolved using the method described in chapter 2 for $\lambda = 1/2$ (4.11a and 4.11b) and $\lambda = 2/3$ (4.11c and 4.11d), $\varepsilon = 1/2$ and a cooling period of $\eta_{\text{cooling}} = 2$. The color represents the value of the field ϕ. Snapshots were taken for conformal times $\eta = 101$ (4.11a and 4.11c) where bubble nucleation in the false vacuum can be clearly observed and $\eta = 751$ (4.11b and 4.11d) where the vacuum has fully decayed.

Chapter 5

Conclusions and future work

We will firstly summarize the results obtain throughout this thesis. Our work followed the same systematic analysis which was validated for the prototypical ϕ^4 potential in chapter 2. In chapter 3 we observed the formation of new types of domain walls outside the range of initial conditions when the field is constrained by a periodic potential. Preliminary results show that the behaviour of these new walls is highly dependent on the expansion rate of the Universe and that it deviates from the analytical model previously validated for a ϕ^4 potential. In sections 4.2 and 4.3 we show that the existence of domain walls in a triple well potential with symmetrical initial conditions and identical minima is unstable and that the field quickly collapses to the central minimum. We try to address this in section 4.4 by introducing a bias between this minimum and the side minima. This proved to be an effective way to provoke the field to decay if, at the same time, we allow the initial conditions to undergo an initial cooling period. This dependence is plotted in figure 4.10.

The results we obtained suggest that the current analytical models that are used to study the evolution of these defects might not be well suited to deal with more exotic potential functions than can naturally occur in the Universe. In any case, it's clear that the evolution of domain walls is always highly dependent on the expansion rate of the Universe regardless of the potential shape.

The most obvious limitation of this thesis was that we had to choose a relatively small box (2048^2) in order to perform an extensive number of simulations for each different case to calibrate and test each model. Since this limits our spatial resolution and the time we can let the simulations run, the statistical accuracy of our results is limited. Whether or not this can account for the deviations to the analytical models is yet to be understood. Another way to increase the resolution and reduce data noise is to increase the number of simulations to be averaged in each model (we used 10). This can be especially useful in better characterizing type-II and type-III walls in a SG potential.

Another interesting extension of these models is to test different initial conditions. In SG this can mean testing how the width in the random distribution of initial conditions affects the exploration of the outer minima. In the simple ϕ^6 case it can be interesting to investigate the

formation and evolution of topological defects if the initial conditions are asymmetrical. This can be also extended to the Christ-Lee potential. Furthermore, since Hindmarsh [17] considers a gaussian distribution for the initial values of the field, it could be interesting to investigate if we can model the vacuum decay using (4.6) by changing this ansatz.

Finally, it can be worth mentioning that a similar analysis to what is presented in this thesis may be a useful benchmark to investigate other topological defects such as strings.

References

[1] N. Aghanim et al. Planck 2018 results. VI. Cosmological parameters. *Astron. Astrophys.*, 641:A6, 2020.

[2] Peter Brockway Arnold and David Wright. The Tricritical point of finite temperature phase transitions in large N (Higgs) gauge theories. *Phys. Rev. D*, 55:6274–6286, 1997.

[3] P. P. Avelino, C. J. A. P. Martins, and J. C. R. E. Oliveira. One-scale model for domain wall network evolution. *Phys. Rev. D*, 72:083506, Oct 2005.

[4] Y. Bergner and Luis M. A. Bettencourt. A Step beyond the bounce: Bubble dynamics in quantum phase transitions. *Phys. Rev. D*, 68:025014, 2003.

[5] Dietrich Bodeker, Lars Fromme, Stephan J. Huber, and Michael Seniuch. The Baryon asymmetry in the standard model with a low cut-off. *JHEP*, 02:026, 2005.

[6] N. H. Christ and T. D. Lee. Quantum expansion of soliton solutions. *Phys. Rev. D*, 12:1606–1627, Sep 1975.

[7] J. R. C. C. C. Correia, I. S. C. R. Leite, and C. J. A. P. Martins. Effects of Biases in Domain Wall Network Evolution. *Phys. Rev. D*, 90(2):023521, 2014.

[8] J. R. C. C. C. Correia, I. S. C. R. Leite, and C. J. A. P. Martins. Effects of biases in domain wall network evolution. ii. quantitative analysis. *Phys. Rev. D*, 97:083521, Apr 2018.

[9] J. R. C. C. C. Correia and C. J. A. P. Martins. General purpose graphics-processing-unit implementation of cosmological domain wall network evolution. *Phys. Rev. E*, 96(4):043310, 2017.

[10] J. R. C. C. C. Correia and C. J. A. P. Martins. Quantifying the effect of cooled initial conditions on cosmic string network evolution. *Phys. Rev. D*, 102(4):043503, 2020.

[11] M. G. do Amaral. φ_2^6 theory on the lattice - an effective potential study. *J. Phys. G*, 24:1061–1076, 1998.

[12] Albert Einstein. Die Feldgleichungen der Gravitation. *Sitzungsberichte der Königlich Preußischen Akademie der Wissenschaften (Berlin*, pages 844–847, January 1915.

[13] Gabriel H. Flores, N. F. Svaiter, and Rudnei O. Ramos. Tunneling and nucleation rate in the $(\frac{\lambda}{4!}\phi^4 + \frac{\sigma}{6!}\phi^6)_3$ model. *International Journal of Modern Physics A*, 14(23):3715–3730, Sep 1999.

[14] A. Friedmann. Über die Krümmung des Raumes. *Zeitschrift fur Physik*, 10:377–386, January 1922.

[15] Alan H. Guth. Inflationary universe: A possible solution to the horizon and flatness problems. *Phys. Rev. D*, 23:347–356, Jan 1981.

[16] Christopher T. Hill and Graham G. Ross. Pseudo-goldstone bosons and new macroscopic forces. *Physics Letters B*, 203(1):125 – 131, 1988.

[17] Mark Hindmarsh. Analytic Scaling Solutions for Cosmic Domain Walls. *Phys. Rev. Lett.*, 77(22):4495–4498, November 1996.

[18] Edwin Hubble. A Relation between Distance and Radial Velocity among Extra-Galactic Nebulae. *Proceedings of the National Academy of Science*, 15(3):168–173, March 1929.

[19] Minu Joy and V. C. Kuriakose. Phase transitions and bubble nucleations for a phi**6 model in curved space-time. *Mod. Phys. Lett. A*, 18:937–946, 2003.

[20] T. W. B. Kibble. Topology of Cosmic Domains and Strings. *J. Phys. A*, 9:1387–1398, 1976.

[21] T. W. B. Kibble. Evolution of a system of cosmic strings. *Nuclear Physics B*, 252:227 – 244, 1985.

[22] Yoonbai Kim, Kei-ichi Maeda, and Nobuyuki Sakai. Monopole bubble in early universe. *Nucl. Phys. B*, 481:453–478, 1996.

[23] A. M. M. Leite and C. J. A. P. Martins. Scaling Properties of Domain Wall Networks. *Phys. Rev. D*, 84:103523, 2011.

[24] Wen-Fa Lu, Guang-Jiong Ni, and Zhi-Guo Wang. Symmetry restoration in two Phi**6 models by quantum effects. *J. Phys. G*, 24:673–681, 1998.

[25] C. J. A. P. Martins. String evolution in open universes. *Phys. Rev. D*, 55:5208–5211, Apr 1997.

[26] C. J. A. P. Martins. *Defect Evolution in Cosmology and Condensed Matter: Quantitative Analysis with the Velocity-Dependent One-Scale Model*. SpringerBriefs in Physics. Springer International Publishing, 2016.

[27] C. J. A. P. Martins and A. Achúcarro. Evolution of local and global monopole networks. *Phys. Rev. D*, 78:083541, Oct 2008.

[28] C. J. A. P. Martins, I. Yu. Rybak, A. Avgoustidis, and E. P. S. Shellard. Extending the velocity-dependent one-scale model for domain walls. *Phys. Rev. D*, 93(4):043534, 2016.

[29] A. Munshi. *OpenCL 1.2 Specification*. Khronos Group Working Group, 19 edition, 2012.

[30] Arno A. Penzias and Robert Woodrow Wilson. A Measurement of excess antenna temperature at 4080-Mc/s. *Astrophys. J.*, 142:419–421, 1965.

[31] S. Perlmutter, G. Aldering, G. Goldhaber, R. A. Knop, P. Nugent, P. G. Castro, S. Deustua, S. Fabbro, A. Goobar, D. E. Groom, I. M. Hook, A. G. Kim, M. Y. Kim, J. C. Lee, N. J. Nunes, R. Pain, C. R. Pennypacker, R. Quimby, C. Lidman, R. S. Ellis, M. Irwin, R. G. McMahon, P. Ruiz-Lapuente, N. Walton, B. Schaefer, B. J. Boyle, A. V. Filippenko, T. Matheson, A. S. Fruchter, N. Panagia, H. J. M. Newberg, W. J. Couch, and The Supernova Cosmology Project. Measurements of Ω and Λ from 42 High-Redshift Supernovae. *Astrophys. J.*, 517(2):565–586, June 1999.

[32] William H. Press, Barbara S. Ryden, and David N. Spergel. Dynamical Evolution of Domain Walls in an Expanding Universe. *Astrophys. J.*, 347:590–604, 1989.

[33] Adam G. Riess, Alexei V. Filippenko, Peter Challis, Alejandro Clocchiatti, Alan Diercks, Peter M. Garnavich, Ron L. Gilliland, Craig J. Hogan, Saurabh Jha, Robert P. Kirshner, B. Leibundgut, M. M. Phillips, David Reiss, Brian P. Schmidt, Robert A. Schommer, R. Chris Smith, J. Spyromilio, Christopher Stubbs, Nicholas B. Suntzeff, and John Tonry. Observational Evidence from Supernovae for an Accelerating Universe and a Cosmological Constant. *Astron. J.*, 116(3):1009–1038, September 1998.

[34] Volker Springel et al. Simulating the joint evolution of quasars, galaxies and their large-scale distribution. *Nature*, 435:629–636, 2005.

[35] A. Vilenkin and E. P. S. Shellard. *Cosmic Strings and Other Topological Defects*. Cambridge University Press, 7 2000.

[36] A. B. Zamolodchikov. Conformal Symmetry and Multicritical Points in Two-Dimensional Quantum Field Theory. (In Russian). *Sov. J. Nucl. Phys.*, 44:529–533, 1986.

[37] F. Zwicky. Die Rotverschiebung von extragalaktischen Nebeln. *Helv. Phys. Acta*, 6:110–127, 1933.


U.PORTO
FACULDADE DE CIÊNCIAS
UNIVERSIDADE DO PORTO